

The TESLA Compton Polarimeter

Vahagn Gharibyan^{1,2}, Norbert Meyners¹, K. Peter Schüler¹

¹DESY, Deutsches Elektronen Synchrotron, Hamburg, Germany

²Yerevan Physics Institute, Yerevan, Armenia

Abstract

This note describes a study of a high-energy Compton beam polarimeter for TESLA. A segment of the beam delivery system has been identified, which is aligned with the e^+e^- collision axis and which has a suitable configuration for high-quality beam polarization measurements. The laser envisaged for the polarimeter is similar to an existing facility at DESY. It delivers very short pulses in the 10 ps, 10 – 100 μ J regime and operates with a pattern that matches the pulse and bunch structure of TESLA. This will permit very fast and accurate measurements and an expeditious tune-up of the spin manipulators at the low-energy end of the linac. Electron detection in the multi-event regime will be the principle operating mode of the polarimeter. Other possible operating modes include photon detection and single-event detection for calibration purposes. We expect an overall precision of $\Delta P/P \sim 0.5\%$ for the measurement of the beam polarization.

Contents

1	Introduction and Overview	2
2	General Considerations	4
2.1	Spin Motion	4
2.2	Suitable Polarimeter Locations	5
2.3	Alignment Tolerances	6
2.4	Beam-Beam Effects	6
3	Compton Polarimetry	7
3.1	Compton Kinematics, Cross Sections, Spin Asymmetry	8
3.2	Potential Background Processes	14
3.3	Compton Detection Methods	14
4	The proposed Compton Polarimeter for TESLA	15
4.1	The Compton IP Region	15
4.2	Spectrometer Magnets	19
4.3	Vacuum Chambers	19
4.4	Electron Detector	20
4.5	Photon Detector Option	22
4.6	Laser System	24
4.6.1	Luminosity for Continuous Lasers	24
4.6.2	Luminosity for Pulsed Lasers	25
4.6.3	Laser Emittance	28
4.6.4	Laser for the Polarimeter	29
4.7	Event Rates and Statistical Errors	30
4.8	Systematic Errors	33
4.8.1	Detector calibration and linearity	33
4.8.2	Laser polarization	34
4.8.3	Cross checks	34
4.9	Infrastructure and Utilities	34
4.9.1	Polarimeter Lab surface building	34
4.9.2	Laser beam transport and diagnostics	36
4.9.3	Tunnel layout	36
4.10	Electronics and Data Acquisition	36
4.11	Cost	37
5	Summary and Conclusion	37
6	Acknowledgments	38

1 Introduction and Overview

A full exploitation of the physics potential of TESLA must aim to employ polarized electron and positron beams with a high degree of longitudinal polarization at full intensity. The technology of polarized electron sources of the strained GaAs type is well established [6, 3, 1] and TESLA is therefore likely to deliver a state of the art polarized electron beam with about 80% polarization from the very beginning. The prospects for the polarization of the positron beam are under investigation. The proposed scheme of Balakin and Mikhailichenko [7, 8, 3, 1] to upgrade the envisaged undulator type positron source of TESLA for the generation of polarized positrons will require R&D before it can be implemented. A positron polarization of 45-60% is expected.

Equally important to the generation of high beam polarization will be its precise measurement and control. The quantity of basic interest is the longitudinal spin polarization of the two beams at the interaction point. Since a precise polarization measurement at the detector IP itself is difficult, the point of measurement should be chosen such that beam transport and beam-beam interaction effects are either negligible or small and well quantified. Other important factors relate to the level of radiation backgrounds and to the technical infrastructure and accessibility of a chosen site.

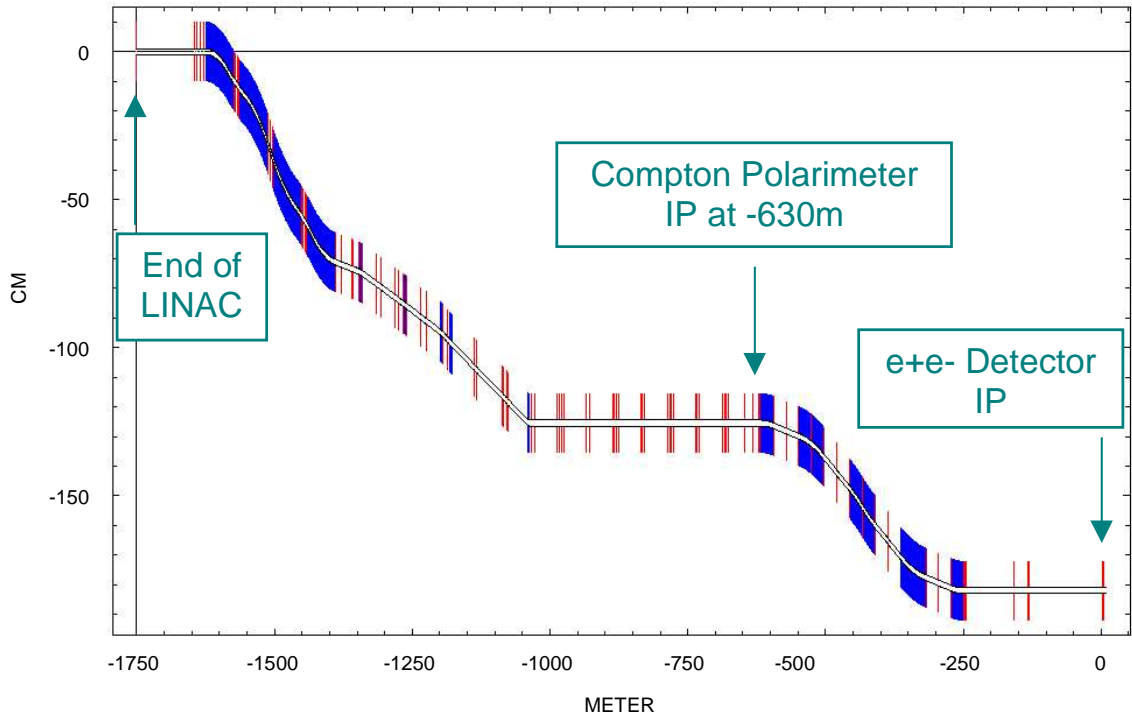


Figure 1. TESLA Beam Delivery System

The concept of the polarimeter that we propose [1, 2] for TESLA is based on the well established laser backscattering method, as it was already envisaged in the TESLA CDR [3, 4]. The proposed location of the Compton IP, where the laser beam crosses the electron or positron beam, is 630 meters upstream of the center of the e^+e^- detector, near the end of a long straight section of the beam delivery system (BDS), see Fig. 1. This part of the beamline is foreseen for general beam diagnosis and is also well suited for high quality beam polarization measurements.

Although the polarization vector experiences large rotations (due to the g-2 effect) as the beam traverses the bends of the BDS, the beam and spin directions at the chosen polarimeter site are precisely aligned, except for a parallel offset, with those at the e^+e^- interaction point. A polarization measurement at the proposed upstream location will therefore provide a genuine determination of the quantity of interest, as long as beam-beam effects are negligible or correctable. This is indeed the case. We estimate the beam-beam induced depolarization at TESLA to be 0.5%.

Fig. 2 shows a layout of the Compton Polarimeter. The laser beam crosses the electron or positron beam with a small crossing angle of 10 mrad at $z = -630$ m, just upstream of a train of ten C-type dipole magnets (BFCH0) which bend the beam horizontally by 0.77 mrad. The Compton scattered electrons are momentum analyzed in the field of the dipoles and detected with a segmented gas Cerenkov counter. An optional calorimetric photon detector can also be employed further downstream.

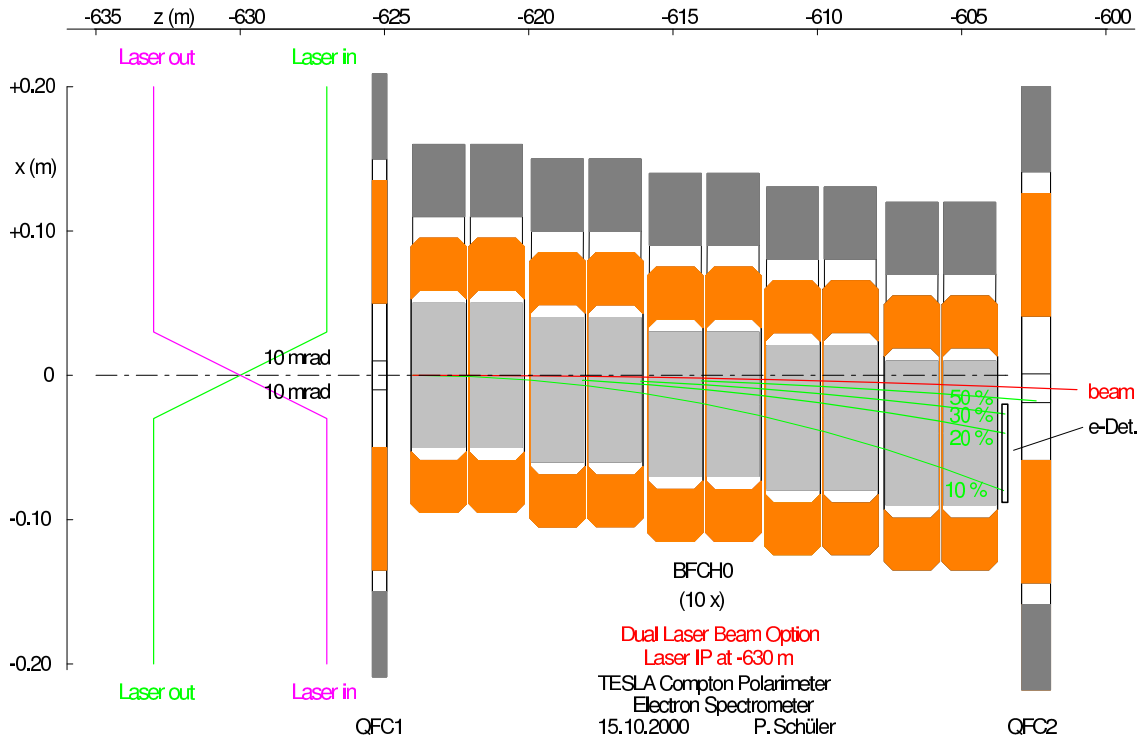


Figure 2. Layout of the Compton Polarimeter

The laser system that we envisage for the polarimeter should be similar to the laser configuration that has been developed by Max Born Institute for the Tesla Test Facility (TTF) photo injector gun at DESY [17, 18]. This laser can be pulsed with a pattern that matches the peculiar pulse and bunch structure of TESLA. In this way it is possible to achieve very high luminosity, typically six orders of magnitude higher than with continuous lasers of comparable average power.

The statistics of Compton produced events is very high to the point where statistical errors will not matter in comparison with systematic errors. We expect a performance similar to the SLD Compton polarimeter at SLAC, with an overall precision of $\Delta P/P \sim 0.5\%$ for the measurement of the beam polarization.

We have also considered the possibility of downstream polarimeter locations, which would in principle permit to investigate beam-beam effects experimentally, as was done with the SLD Compton polarimeter at SLAC. However, the envisaged geometry of the extraction beamline at TESLA appears to be very unfavorable for beam polarimetry.

2 General Considerations

Before we turn to the details of our Compton polarimeter proposal for TESLA, we will address several general as well as specific topological features of the accelerator which may have an impact on beam polarimetry. We start with an analysis of the expected spin motion effects along the machine, which will then naturally lead to a discussion of suitable polarimeter sites and alignment tolerances. The expected degree of depolarization from the beam-beam interaction will also be investigated.

2.1 Spin Motion

The spin motion of a deflected electron or positron beam in a transverse magnetic field follows from the familiar Thomas-Larmor expression

$$\theta^{spin} = \gamma \frac{g-2}{2} \theta^{orbit} = \frac{E_0}{0.44065 \text{ GeV}} \theta^{orbit} \quad (1)$$

where θ^{orbit} and θ^{spin} are the orbit and spin deflection angles, E_0 is the beam energy, $\gamma = E_0/m$, and $(g-2)/2$ is the famous g-factor anomaly of the magnetic moment of the electron.

In Table 1 we have listed the major orbit deflection angles of the TESLA linac, the beam delivery and extraction systems, and the associated spin rotation angles for a beam energy of 250 GeV.

The electron linac starts tangential to HERA with a negative slope of -8 mrad and turns level after some 3 km. From there on, the elevation of the tunnel follows the equipotential curvature of the earth (see Fig. 8.2.3 of the TDR). Over the entire 33 km length of TESLA, the curvature of the earth alone generates a directional change of 3.2 mrad in the orbit, which results in a large vertical spin rotation angle of 104° at 250 GeV. The beam delivery system, which begins 1.65 km upstream of the e^+e^-

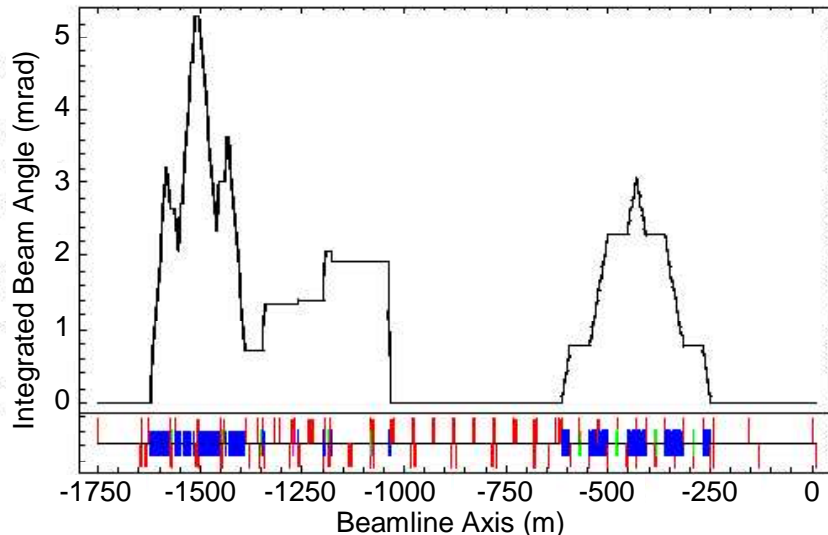


Figure 3. Bend angles of the TESLA Beam Delivery System

interaction point, see Fig. 1, subjects the beam to a succession of horizontal deflections as shown in Fig.3.

Downstream from the detector, the beam extraction system generates a vertical deflection of -15 mrad, which leads to the beam dump.

Even modest orbit deflections of a few millirad will result in large spin rotations, as can be appreciated by looking at the last two columns of Table 1. At a beam energy of 400 GeV, the spin rotation angles are even larger (by a factor of 1.6).

In order to obtain useful longitudinal spin orientation at the experiment, the spin vector must be injected into the linac with an angular tilt that will compensate the net spin motion effects on the way to the interaction point. This is best done with a spin manipulator at the exit of the damping ring.

2.2 Suitable Polarimeter Locations

There are several upstream beamline locations where the beam axis is nominally parallel to the interaction and detector axis at $z = 0$:

- (1) **Upstream of the detector** ($z \simeq -200 \dots -20 \text{ m}$).

This is the part of the final focus and final telescope system, where the beamline coincides with the detector axis. While a laser beam crossing is conceivable in this section, there is no practical way to separate and detect the scattered Compton particles, except maybe for some limited electron detection in the beam extraction region downstream of the physics detector.

- (2) **The long straight section of the BDS** ($z \simeq -1042 \dots -624 \text{ m}$).

This part of the beamline is precisely aligned with the collision axis, except for a parallel offset, which separates the beam from beamstrahlung of the other beam. This sector is

foreseen for general beam diagnosis and is also well suited for high quality polarization measurements. A train of dipole magnets at the end of this straight section deflects the charged beam by 0.77 mrad. The configuration of these dipole magnets can be adjusted to serve as a magnetic spectrometer for the Compton scattered electrons. Photon detection is also possible. Although the area of interest is slightly outside of the Ellerhoop site boundaries in the case of the e^- polarimeter, it is nevertheless very close to conceivable laser and electronics facilities on the surface.

(3) The end of the linac ($z \simeq -1750 \dots -1650 \text{ m}$).

The beamline at this location has a slight vertical tilt of 0.1 mrad with respect to the collision axis, due to the curvature of the earth over this distance, which corresponds to a spin rotation angle of 3.3° at 250 GeV (see Table 1). This area will also be congested by equipment from the positron source and its associated undulator. A laser beam transport to this site with a length of 1 km is not practical and a laser in situ in the tunnel is also not attractive for reliability reasons.

- We came to the conclusion that the second location is the best choice.

We have also considered the possibility of downstream polarimeter locations, which would in principle permit to investigate beam-beam effects experimentally, as was done with the SLD Compton polarimeter at SLAC. However, the envisaged geometry of the extraction beamline at TESLA appears to be very unfavorable for beam polarimetry.

2.3 Alignment Tolerances

In order to guarantee that the polarization measurement $\Delta P/P$ at the chosen polarimeter site does not suffer from systematic misalignments of the beam direction via Equation 1, we will postulate the following alignment tolerances

$$\begin{aligned} \Delta P/P \leq 0.1\% \quad \longrightarrow \quad \Delta\theta^{spin} \leq 45 \text{ mrad} \quad \longrightarrow \quad \Delta\theta^{orbit} \leq 80 \mu\text{rad} \quad (250 \text{ GeV}) \\ \longrightarrow \quad \Delta\theta^{orbit} \leq 50 \mu\text{rad} \quad (400 \text{ GeV}) \end{aligned}$$

The beam direction at the polarimeter site should therefore be aligned with the collision axis at the e^+e^- interaction point to within $50\mu\text{rad}$. While such an alignment tolerance over a distance of about 600m is not entirely trivial, it is well within the alignment requirements of TESLA.

2.4 Beam-Beam Effects

The strong beam-beam interaction at the collider IP will diffuse the angular spread of the beam. In Table 2 we have listed the rms values of the orbital angular spread of the disrupted beams at TESLA as obtained by O. Napoly. From the orbital rms values we have determined the associated rms spin distribution angles according to Equation 1 which are also listed in Table 2.

	z (km)	$\Delta\theta_x^{orbit}$ ($mrad$)	$\Delta\theta_y^{orbit}$ ($mrad$)	$\Delta\theta_x^{spin}$ (deg)	$\Delta\theta_y^{spin}$ (deg)
e^- linac					
front of linac	-16.5	0.0	-5.6	0^0	-3.6^0
end of vert. slope	-13.5	0.0	2.0		14^0
end of linac	-1.65	0.0	0.1	0^0	3.3^0
BDS					
5.3 mrad	-1.523	5.295		172^0	
front of straight section	-1.042	0.000	0.000	0^0	0^0
end of straight section	-0.624	0.000	0.000	0^0	0^0
3 mrad	-0.442	3.067	0.000	100^0	0^0
dump hall	-0.258	0.000	0.000	0^0	0^0
detector region					
e^+e^- IP	0.000	0.000	0.000	0^0	0^0
beam extraction region					
ESEP, MSEP, BV	0.110	0.0	-15	0^0	-500^0

Table 1: Orbit and spin rotation angles at 250 GeV. All angles are relative to the e^+e^- detector axis. For 400 GeV multiply all spin rotation angles of this table by 1.6.

Based on these numbers, we estimate the overall depolarization of the spent beam to be $\Delta P/P \simeq 1 - \cos(139mrad) = 1\%$, independent of beam energy. Assuming that the beam-beam interaction proceeds in a symmetric fashion upstream and downstream from the IP, we estimate the effective depolarization of the beam before the IP to be half of the overall effect, i.e. 0.5%.

	$\Delta\theta_x^{orbit}(rms)$ (μrad)	$\Delta\theta_y^{orbit}(rms)$ (μrad)	$\Delta\theta_x^{spin}(rms)$ ($mrad$)	$\Delta\theta_y^{spin}(rms)$ ($mrad$)
250 GeV	245	27	139	15
400 GeV	153	17	139	15

Table 2: Disrupted beam rms angular spreads of orbit and spin angles.

3 Compton Polarimetry

Before we cover the technical details of our polarimeter proposal, we review briefly some of the basic features of the Compton scattering process.

3.1 Compton Kinematics, Cross Sections, Spin Asymmetry

The Compton kinematics are characterized by the dimensionless variable

$$x = \frac{4E_0\omega_0}{m^2} \cos^2(\theta_0/2) \simeq \frac{4E_0\omega_0}{m^2} \quad (2)$$

where

- E_0 is the initial electron energy,
- ω_0 is the initial photon energy,
- m is the mass of the electron,
- θ_0 is the crossing angle between the electron beam and the laser.

Note that $\cos^2(\theta_0/2) \simeq 1$ in most practical polarimeter cases.

The energies of the scattered photon and the scattered electron, ω and E , are related through energy conservation

$$\omega + E = \omega_0 + E_0 \simeq E_0 \quad (3)$$

The scattered photon and the scattered electron angles relative to the electron beam direction are

$$\theta_\gamma = \frac{m}{E_0} \sqrt{\frac{x}{y} - (x+1)} \quad (4)$$

$$\theta_e = \frac{y}{1-y} \theta_\gamma \quad (5)$$

where

$$y = 1 - \frac{E}{E_0} = \frac{\omega}{E_0} \quad (6)$$

is the normalized energy variable of the scattered photon.

The spin-dependent differential Compton cross section is

$$\frac{d\sigma}{dy} = \frac{2\sigma_0}{x} \left[\frac{1}{1-y} + 1 - y - 4r(1-r) + P\lambda r x(1-2r)(2-y) \right] \quad (7)$$

where P is the initial electron helicity ($-1 \leq P \leq +1$), λ is the initial photon helicity ($-1 \leq \lambda \leq +1$), and

$$\sigma_0 = \pi r_0^2 = 0.2495 \text{ barn} \quad (8)$$

$$r = \frac{y}{x(1-y)} \quad (9)$$

The energy spectra of the scattered photon and electron are mirror images of each other because of equation 3. The spectra are continuous and extend to the so-called Compton edge, which corresponds to a maximum energy of the scattered photon and a minimum energy of the scattered electron

$$\omega_{max} = E_0 \frac{x}{1+x} \quad (10)$$

$$E_{min} = E_0 \frac{1}{1+x} \quad (11)$$

In Table 3 we have listed these energy limits for several laser and electron beam energy configurations.

The spin asymmetry or analyzing power is defined as

$$A = \frac{d\sigma^- - d\sigma^+}{d\sigma^- + d\sigma^+} \quad (12)$$

where the $(-)$ and $(+)$ denote opposite and like sign helicity configurations of the two beams with $P\lambda = \pm 1$. The opposite sign helicity configuration ($P\lambda = -1$), which has parallel spins ($m_j = 3/2$), dominates at the Compton edge over the other helicity and spin orientation ($P\lambda = +1$ and $m_j = 1/2$). The asymmetry, as defined here, is therefore positive at the Compton edge.

The asymmetry changes sign at the crossover points

$$\omega_c = E_0 \frac{x}{2+x} \quad (13)$$

$$E_c = E_0 \frac{1}{1+x/2} \quad (14)$$

which coincide with the point where the maximum electron scattering angle is attained.

For Compton detection in the multi-photon mode, which will be discussed in Chapter 3.3 and 4.5, it is convenient to define a multi-photon asymmetry or analyzing power

$$A_p = \frac{I^- - I^+}{I^- + I^+} \quad (15)$$

where I^- and I^+ are the integrals of the energy weighted photon spectra

$$I^\pm = \int y \frac{d\sigma^\pm}{dy} dy \quad (16)$$

and the $(-)$ and $(+)$ signs denote helicity configurations as before.

The energy spectra, the associated spin asymmetry and the scattering angles of the Compton scattered electrons and photons are shown in Fig. 4 for a beam energy of 250 GeV and a green laser (2.33 eV). This configuration allows for good coverage of the most interesting part of the electron spectrum with the spectrometer that will be described in Chapter 4.2.

For much higher or lower beam energies, it will be advantageous to change the wavelength of the laser. The corresponding spectra for 400 GeV (1.165 eV) and 45.6 GeV (4.66 eV) are given in Fig. 5 and 6.

The multi-photon analyzing power A_p is also indicated in these figures. Its energy dependence is shown in Fig. 10.

E_0 (GeV)	λ (nm)	ω_0 (eV)	x	ω_{max} (GeV)	E_{min} (GeV)
45.6	1064	1.165	0.813	20.4	25.2
	532	2.33	1.63	28.3	17.3
	266	4.66	3.25	34.9	10.7
250	1064	1.165	4.46	204	46
	532	2.33	8.92	225	25
	266	4.66	17.8	237	13
400	1064	1.165	7.14	351	49
	532	2.33	14.3	374	26
	266	4.66	28.6	386	14

Table 3: Kinematic parameters for several laser and beam energy configurations.

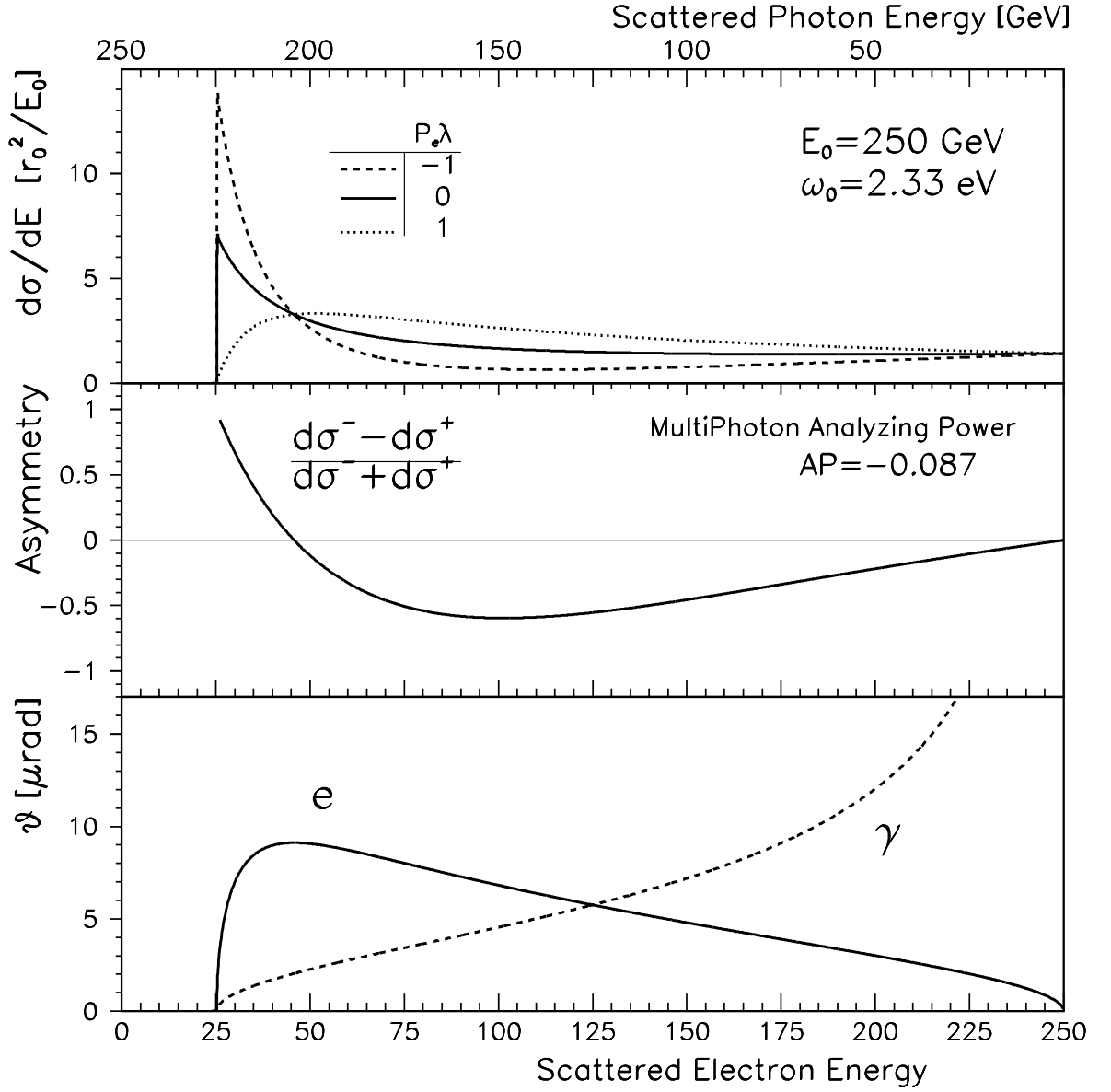


Figure 4. Energy spectra (top), spin asymmetry (middle) and scattering angles (bottom) of Compton scattered electrons and photons, for a beam energy of 250 GeV and a green laser.

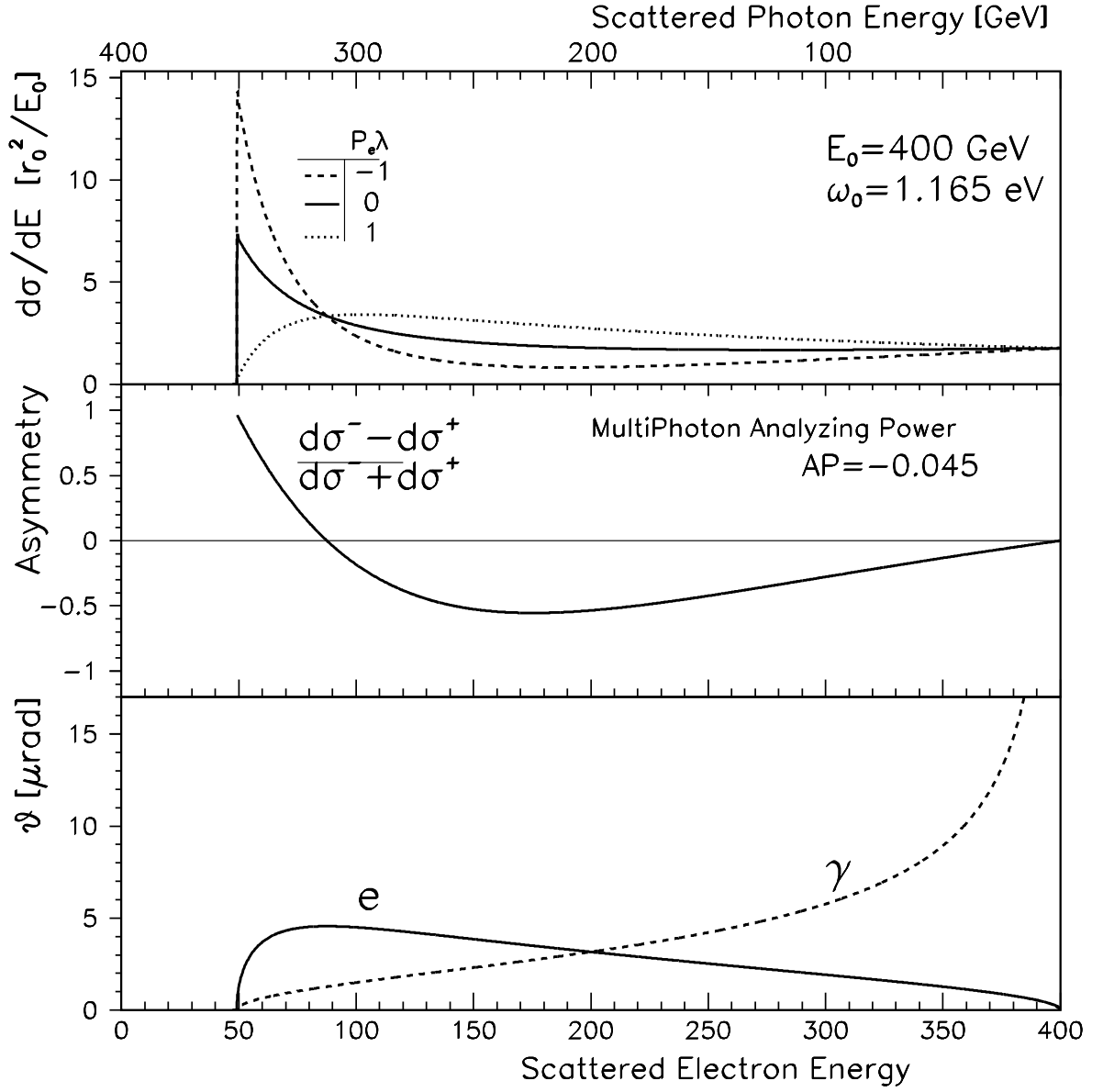


Figure 5. Energy spectra (top), spin asymmetry (middle) and scattering angles (bottom) of Compton scattered electrons and photons, for a beam energy of 400 GeV and an infrared laser.

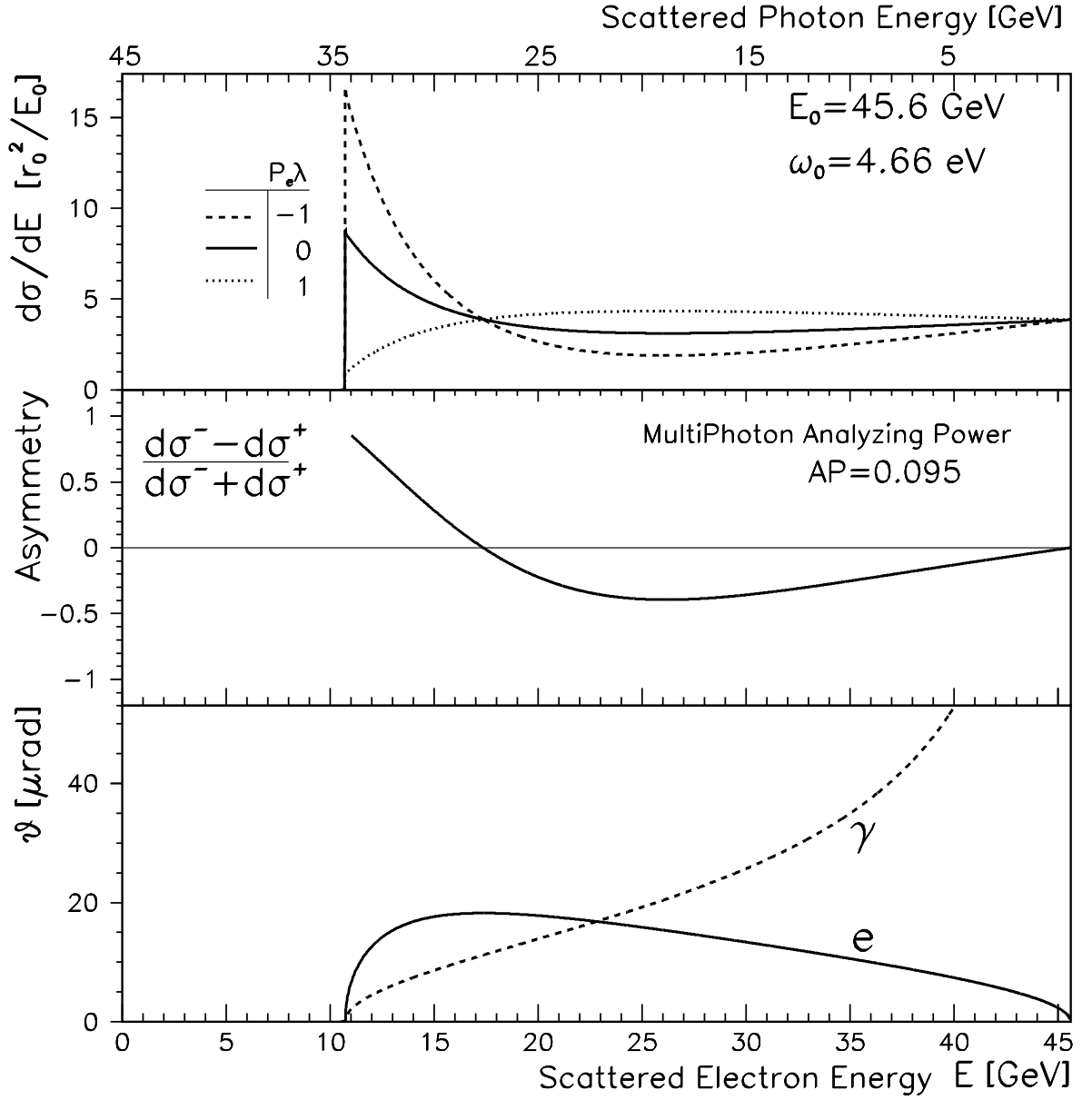


Figure 6. Energy spectra (top), spin asymmetry (middle) and scattering angles (bottom) of Compton scattered electrons and photons, for a beam energy of 45.6 GeV and an ultraviolet laser.

3.2 Potential Background Processes

We will consider here briefly three processes which can in principle interfere with the Compton scattering process $\gamma e \rightarrow \gamma e$. Two of these are open only above a characteristic threshold in x [9, 10], the third is bremsstrahlung from the residual gas in the beam pipe.

(1) $\gamma\gamma \rightarrow e^+e^-$ (two-step conversion)

where one of the two photons originated from a prior Compton event which then interacts with another laser photon. This channel has a threshold of $x = 4.83$ and is therefore in principle open for many of the configurations listed in Table 3. However, as a two-step process, it requires extremely high photon densities in the laser focus to be significant. For the polarimeter conditions of interest to us, we may safely ignore this process.

(2) $\gamma e \rightarrow e e^+e^-$ (direct pair production)

This channel is a higher order QED correction which has a threshold at $x = 8$. Corrections to the analyzing power of Compton polarimeters have been calculated [11, 12, 13]. These corrections are $\leq 0.5\%$ for the polarimeter conditions of interest to us.

(3) $eX \rightarrow eX\gamma \rightarrow eXe^+e^-$ (beam gas background)

Assuming a residual gas pressure of $5 \cdot 10^{-9}$ mbar of CO and an effective length of 375 m for the straight section upstream of the polarimeter, we have $6 \cdot 10^{-12}$ of a radiation length. For typical TESLA parameters with $2 \cdot 10^{10}$ electrons per bunch, we estimate a bremsstrahlung background of 0.05 electrons per bunch in the polarimeter electron detector, and 1 photon per bunch in the optional photon detector (see chapters 4.4 and 4.5). In comparison, with the pulsed laser system that we propose, we expect of order 10^3 Compton events per bunch. We conclude that beam gas background will not be a problem.

3.3 Compton Detection Methods

The kinematics of the Compton scattering process $\gamma e \rightarrow \gamma e$ is completely determined if the momentum vector and identity of only one of the two final state particles is obtained, in addition to the known initial state conditions. In the single-event regime, where individual Compton events originate from separate accelerator bunches, it would be more or less equivalent to measure either the scattered high energy photon or the scattered electron, in order to reconstruct the full kinematic signature of the event.

The experimental conditions may require, however, to operate with short and intense laser pulses and very high instantaneous event rates, where the detector signals are superpositions of multiple events. This may be necessary when the pulse repetition rate of the accelerator or laser is too low to accumulate sufficient statistics from single events. This condition applied to the SLD Compton polarimeter [5] at SLAC, where the bunch rate of the accelerator was 120 Hz and the laser pulse rate even less at 17 Hz.

The bunch crossing frequency of TESLA is about 1/1000 that of the HERA storage ring and the same relationship holds for the average electron currents. At TESLA it will therefore be necessary to compensate the lower electron current by boosting the

useful photon flux of the laser, in order to match the statistical performance of the HERA beam polarimeters [14, 15]. It is then unavoidable to operate in the multi-event regime where the detector response signal of many superimposed Compton events is recorded for each bunch.

In this multi-event regime, however, photon detection is no longer equivalent to electron detection, as the individual events and their kinematic signatures cannot be disentangled. The photon detector signal will likely be an energy weighted integral over the entire photon spectrum. This integral multi-photon analyzing power will be relatively low. Nevertheless, the performance of the LPOL polarimeter [15] at HERA, which is based on this method, demonstrates that this approach can be quite successful.

The SLD Compton polarimeter [5], in contrast, is primarily based on electron detection. The electron detector is configured as a segmented device behind a dispersive field region. This approach has the advantage that regions of high analyzing power can be selected and the shape of the spectrum can be monitored even under multi-event conditions.

For the TESLA Compton polarimeter, we plan to employ electron detection in the multi-event regime as the principle detection method. We will, however, reserve the multi-photon detection method as an option, see Ch. 4.5, especially for TESLA operation at the Z-pole.

Furthermore, we would like to point out that it can be very useful for calibration purposes to operate occasionally in the single-event regime, either with reduced pulse power of the laser or even with cw lasers.

4 The proposed Compton Polarimeter for TESLA

The general features of the proposed Compton polarimeter were already outlined in Chapter 1. We will now describe the major components.

4.1 The Compton IP Region

The topology of the Compton interaction region must be carefully evaluated, as it affects the performance of the polarimeter in several ways. We shall consider only geometries with small, but non-zero, crossing angle. The relevant expressions for the Compton luminosity will be given in Ch. 4.6.

(1) Location of the IP along the beamline.

In order to maximize the Compton signal, the laser should usually cross at or near a waist of the electron beam. The TESLA beam profile in the region of interest is shown in Fig. 7. The beam diameter has a minimum at $z = -625 \text{ m}$. There were three quadrupole magnets (QFB5, QFB6 and QFC1) in the original optical lattice which would have interfered with a laser beam crossing at this position. The transverse dimensions of the electron beam remain, however, quite excellent over an extended region around the waist location.

In order to evaluate potentially adverse effect of the quadrupoles on the scattered electron trajectories, we have propagated simulated Compton electrons through the magnets to the location of the electron detector. Fig. 8a shows a scatter plot at this location for Compton events originating at $z = -624.5 \text{ m}$, downstream of the quadrupoles. Fig. 8b gives the situation for an origin at $z = -632.5 \text{ m}$, which is upstream of the quadrupoles. Although the vertical spread is twice as large for the upstream IP location ($\pm 0.2 \text{ mm}$), it is still very small and well within the acceptance and resolution of the detector. In fact, most of the difference is not due to the quadrupoles, but from the additional 8m of drift space.

In the course of this study, we learned (from O. Napoly) that two of these quadrupoles (QFB5 and QFB6) are still "inactive" in the current TESLA beam optics and that they may be relocated elsewhere, if they interfere with our polarimeter design.

- We have therefore removed these quadrupoles (QFB5, QFB6) to make room for a laser beam crossing at this location (IP at $z = -630 \text{ m}$).

(2) Choice of the crossing angle.

The luminosity depends also on the crossing angle of the two interacting beams. For a continuous laser beam, the luminosity is inversely proportional to the crossing angle, which appears to favor very long beam crossing chambers. The TPOL polarimeter [14] at HERA operates with a crossing angle of 3 mrad and a distance of 15 m between the final input mirror and the focus at the IP. However, one needs to consider also the size of the laser focus, which increases with focal length and thus effectively eliminates the perceived advantage of a very small crossing angle.

For a pulsed laser with very short ($\simeq 10 \text{ ps}$) pulses, the beam crossing angle determines the degree of sensitivity of the luminosity to the relative timing of the two interacting beams, and also to the laser pulse length itself, in the sense that these tend to become less critical for small crossing angles.

Here again the benefit of a small crossing angle must be balanced against the loss associated with an enlarged laser focus. A quantitative analysis must consider the wavelength dependent emittance of the laser, the pulse length and time jitter of the laser, the geometry of the electron beam pipe and the laser beam optics.

Based on conservative assumptions, we conclude that a beam crossing angle of 10 mrad is a good choice for the TESLA Compton polarimeter.

(3) Vertical vs. horizontal crossing.

As the size of the laser focus dominates over the TESLA electron beam size, it does not matter in terms of luminosity, whether we choose vertical or horizontal beam crossing. We prefer vertical beam crossing, as we expect less radiation exposure to the optical elements above and below the electron beamline.

(4) Beam crossing chamber.

A conceptual layout of the vacuum chamber at the Compton IP is given in Fig. 14 in the Appendix. Please note the very different transverse and longitudinal scales. This

design can accommodate two laser beams. The insertion and exit mirrors are 3 m away from the IP. The mirror centers are 30 mm above or below the electron beam axis. The laser beams enter and exit through optical windows which separate the accelerator and the laser beam pipe vacuum.

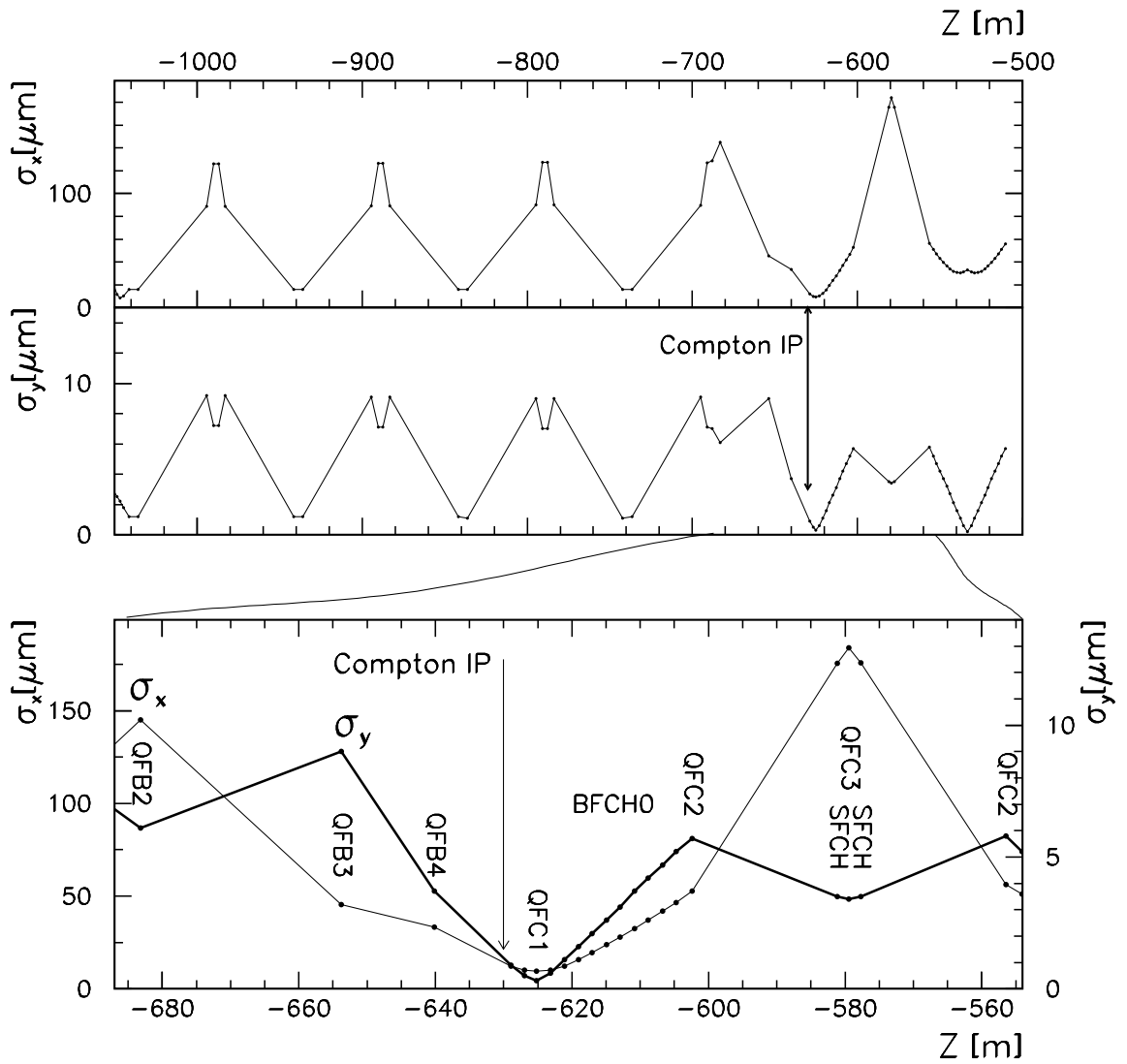


Figure 7. The BDS beam profile.

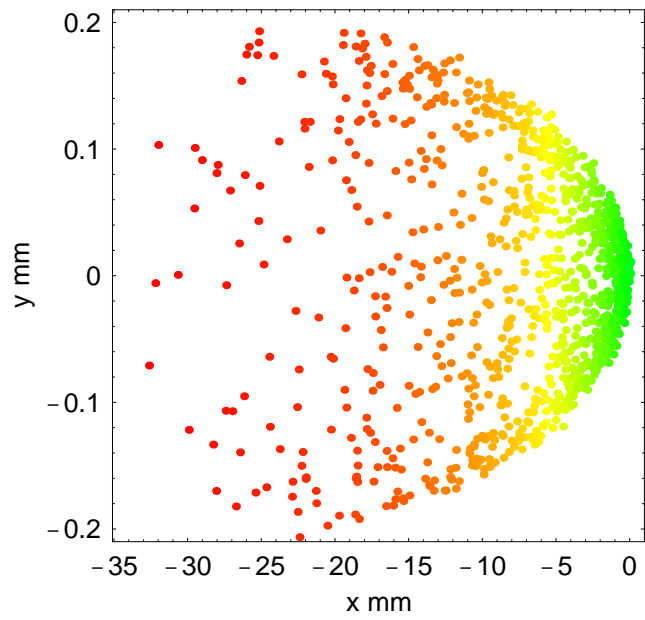
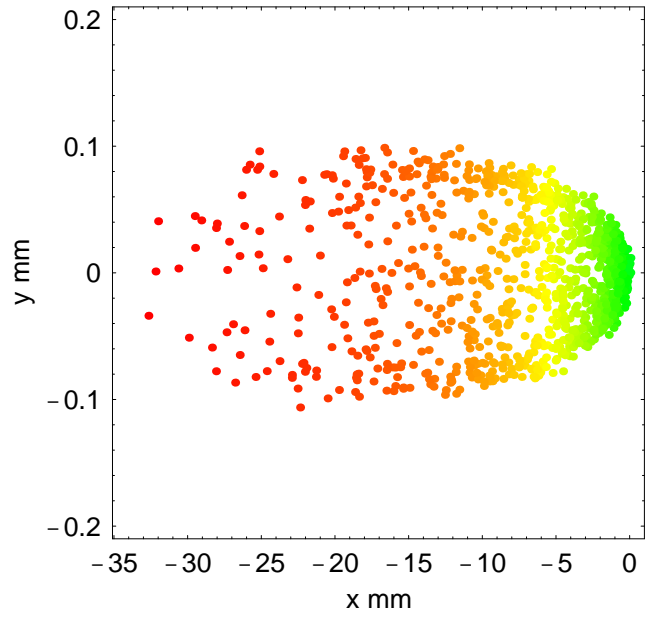


Figure 8. Compton electron scatter plots:
(a) Compton IP at -624.5 m (top),
(b) Compton IP at -632.5 m (bottom).

4.2 Spectrometer Magnets

The group of ten C-type dipole magnets BFCH0 ($z = -624 \dots -604 \text{ m}$) at the end of the long BDS straight section bend the TESLA beam horizontally by 0.77 mrad . Fig. 13 shows an engineering drawing of this magnet. The iron yoke of each dipole has a length of 1.8 m , with a yoke to yoke spacing between adjacent elements that alternates between 0.2 and 0.3 m .

Since the gap of these dipole magnets is relatively wide ($20\text{mm} \times 100\text{mm}$), they are suitable as spectrometer magnets for the scattered Compton electrons. In order to cover a wide range of momenta, we propose to adjust the lateral position of the individual magnets in four steps of 10 mm , as indicated in Fig. 2. In this way we can cover scattered electron momenta down to 10% of the beam momentum, without leaving the good field region. Towards higher momenta we can reach up to 40%, at which point the trajectory is separated by 20 mm from the neutral beam axis, and by 12 mm from the charged beam axis, which is just outside the nominal beam pipe radius of 9.5mm .

Actually, it will be advantageous to have special vacuum chambers, inside the magnets as well as downstream, in order to facilitate the undisturbed exit and detection of the Compton scattered electrons and photons. This will be discussed in the following chapter.

In order to describe the performance of the spectrometer in a quantitative way, we give the lateral dispersion x_d of the electron trajectories for a nominal detector position at $z_d = -603.5 \text{ m}$

$$x_d = -\frac{E_0}{E} \cdot 8.026 \text{ mm} \quad (17)$$

4.3 Vacuum Chambers

The Compton polarimeter will require several special vacuum chambers:

(1) Beam crossing chamber at the Compton IP.

This chamber, which facilitates the crossing of the laser and electron beams, was already discussed in Chapter 4.1. A conceptual design is shown in Fig. 14 of the Appendix.

(2) Dipole vacuum chambers.

In order to accommodate the trajectories of the degraded electrons, the dipole magnets must be outfitted with special vacuum chambers of rectangular profile. The walls must be heavy (3 mm SS-316) to resist flexure due to the outside air pressure. The width of the rectangular profiles should be increased in steps from a minimum 40 mm for the first two dipoles, to a maximum of 110 mm for the last two dipoles. A conceptual engineering design is shown in Fig. 15 in the Appendix. The individual chambers will be 2m long, with short bellows joints every 4m.

(3) Electron exit vacuum chamber.

The geometries of the exiting electron trajectories and the electron detector array (see Fig. 9) require a special chamber which allows a very close approach to the beam. Fig. 16 in the Appendix shows a conceptual engineering design of such a chamber

(4) Photon exit beam pipe.

The Compton scattered photons emerge at very small angles ($\simeq 10 \mu rad$) against the original electron beam direction upstream of the magnets and propagate therefore essentially straight along the neutral beam axis, while the charged beam is deflected by $0.77 mrad$, as shown in Fig. 11. We have indicated the neutral beam offset in the downstream quadrupole and sextupole magnets in Fig. 17-20 in the Appendix. The photons emerge within the horizontal gaps between the pole pieces and the coils.

It will require a special electron beam pipe with a horizontal bulge, at least through the first quadrupole QFC2, to prevent the photons from striking the wall of the pipe. Further downstream, the photons could exit the electron vacuum through a metallic window and travel in their own vacuum of lesser quality.

4.4 Electron Detector

Our conceptual design of the electron detector array is modeled after the multi-channel gas Cerenkov detector of the SLD Compton polarimeter [5], but differs somewhat in the topology of the light guides and the phototubes. Fig. 9 shows the conceptual layout. The array consists of 14 gas Cerenkov channels of rectangular cross section ($5 mm$ wide x $10 mm$ high x $150 mm$ long) which are lined up with the incoming electron trajectories. The channels are made from thin-walled stainless steel which is coated with aluminum on the inside for efficient reflection of the Cerenkov light. At the end of the Cerenkov radiator, the light is reflected through 90° and propagates through a continuation of the channel that functions as a light guide to the phototube.

The detector array is mounted on a movable table with remote control. In this way it is possible to cross-calibrate the different channels against each other. A special electron exit vacuum chamber allows to place the detector very close to the beam. The entire structure is enclosed by shielding, except for a narrow beam entry slot.

The SLD polarimeter group used propane gas (at a slight overpressure of 1.1 atm) with a Cerenkov threshold for relativistic electrons of about 10 MeV. This type of detector is immune to low energy and diffuse background and therefore well suited to operate under severe background conditions.

Instead of propane, we plan to employ C_4F_{10} gas, which has a similar threshold, but is non-flammable. To insure that the gas quality does not deteriorate with time, it may be necessary to circulate the gas through the system.

The momentum coverage and binning of the detector array has been evaluated with Equation 17 and is shown in Table 4.

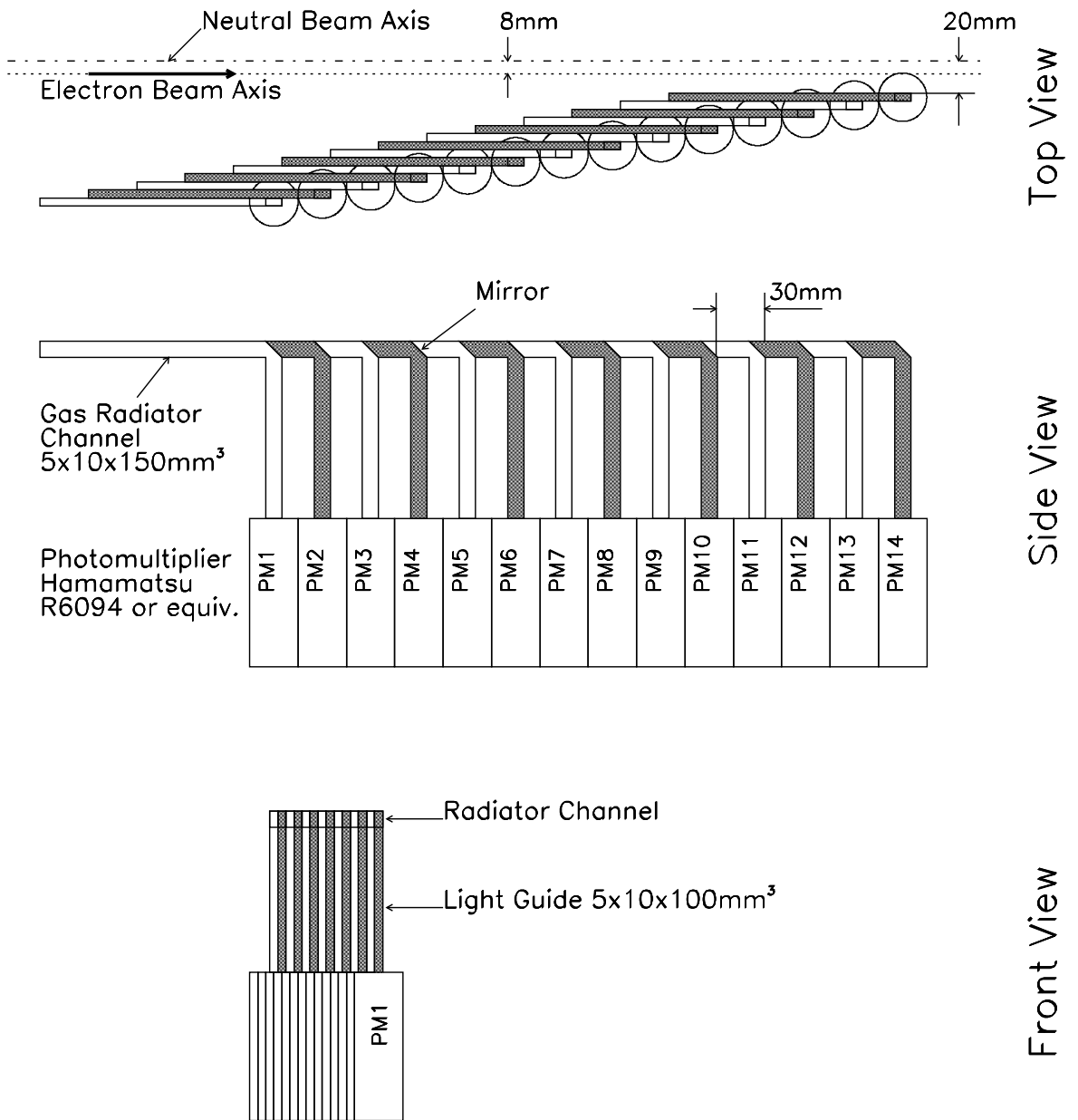


Figure 9. The Electron Detector

<i>bin</i> #	min x_d (mm)	max x_d (mm)	E/E_0 low	E/E_0 high
1	-85	-90	0.089	0.094
2	-80	-85	0.094	0.100
3	-75	-80	0.100	0.107
4	-70	-75	0.107	0.115
5	-65	-70	0.115	0.123
6	-60	-65	0.123	0.134
7	-55	-60	0.134	0.146
8	-50	-55	0.146	0.161
9	-45	-50	0.161	0.178
10	-40	-45	0.178	0.201
11	-35	-40	0.201	0.229
12	-30	-35	0.229	0.268
13	-25	-30	0.268	0.321
14	-20	-25	0.321	0.401

Table 4: Energy coverage and binning of the electron detector array.

4.5 Photon Detector Option

The electron detection method should be sufficient to provide high quality polarization measurements for all conceivable operating conditions of TESLA. At very low beam energy, however, as would be required for running at the Z-pole, it would be necessary to operate the laser and the laser beam transport in the ultraviolet, in order to cover a reasonable fraction of the electron energy spectrum (see Fig. 6).

If the photon detection option is realized, it will not be necessary to operate the laser at such a low wavelength, since the multi-photon asymmetry A_p defined in Equation 15 will be quite large with visible and even infrared laser operation at 45.6 GeV. This can be seen in Fig. 10, which shows A_p as a function of beam energy for three laser photon energies: 1.165 eV (IR), 2.33 eV (green), and 4.66 eV (UV).

Photon detection, in addition to electron detection, will also be useful as it provides another measurement of the beam polarization that can serve as a check. Furthermore, with very much reduced laser pulse power or with cw lasers, it will be possible to do occasional coincidence measurements with both detectors. While such measurements will be relatively slow, they will provide very powerful constraints for systematic investigations.

A calorimetric photon detector can be placed adjacent to the electron beam pipe at $z=-560$ m, as shown in Fig. 11, about 40m downstream from the end of the dipole spectrometer and the electron detector. The high-energy Compton photons do not actually strike the quadrupole and sextupole magnets near $z = -580$ m, as could be inferred from Fig. 11, but pass through a gap between the pole pieces and the coils.

Compton Polarimeter MultiPhoton Mode

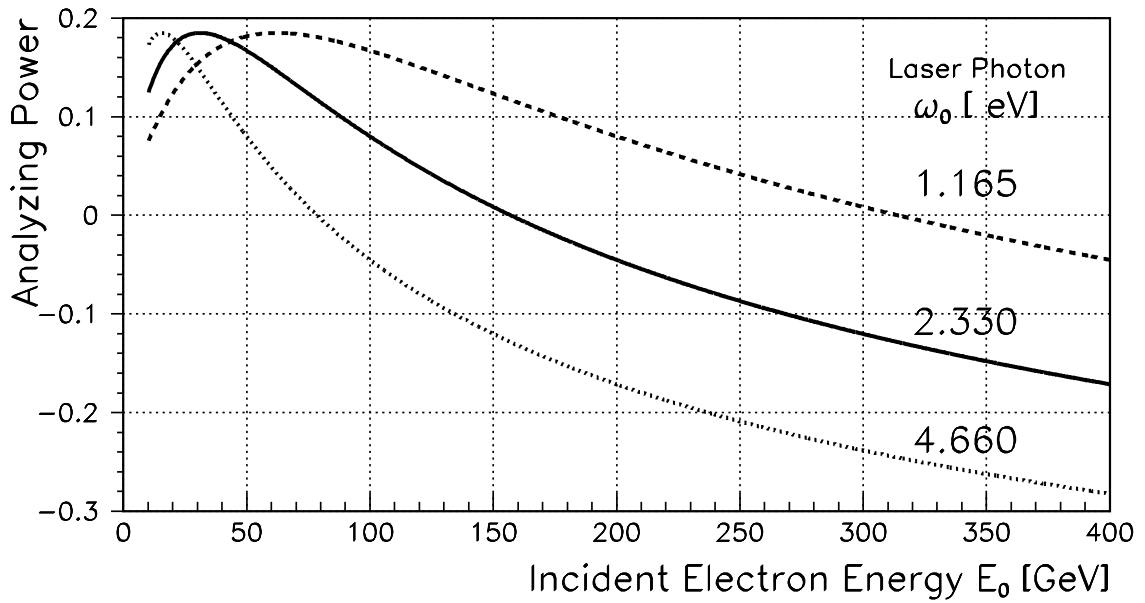


Figure 10. The multi-photon analysing power.

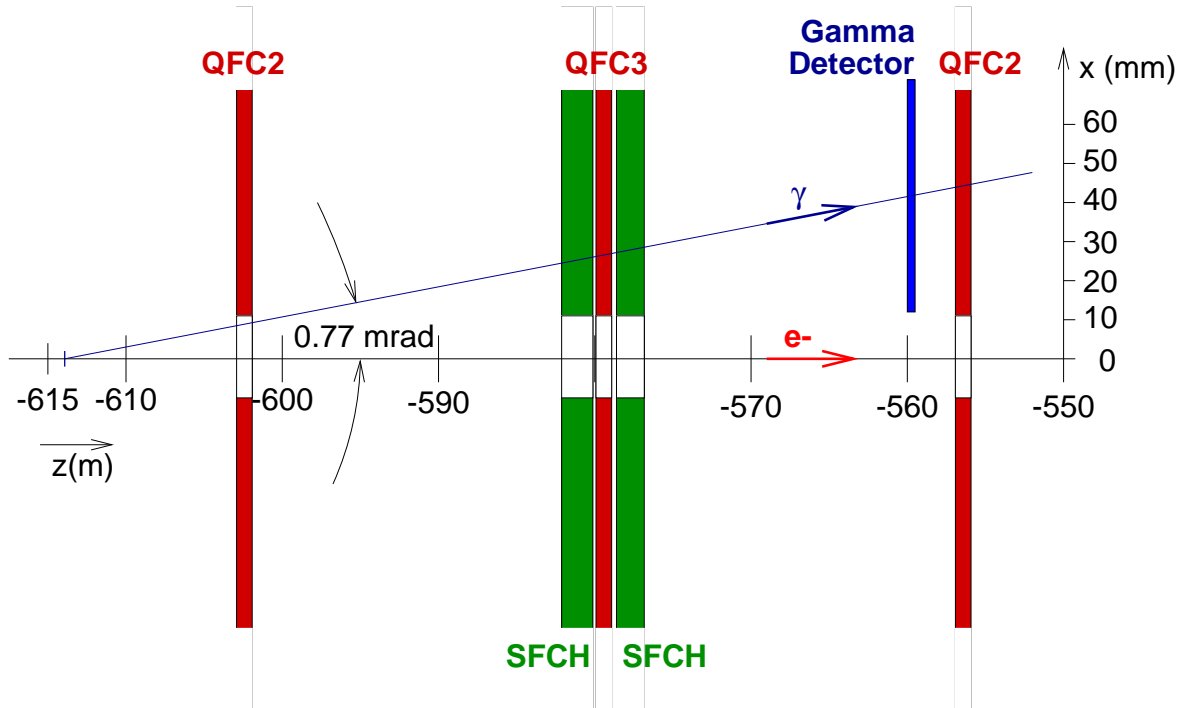


Figure 11. The photon detector option.

See also Fig. 17-20 for additional detail. The main challenge will be to construct a suitable electron beam pipe and exit window to extract the photons. This was already discussed in Chapter 4.3.

The photon calorimeter itself could be relatively simple, as it only needs to measure the total energy deposit in the multi-photon mode with good linearity. The calorimeter material should be radiation hard to survive a Compton bombardment at about $10^7 Hz$, if the laser is operated at full power.

4.6 Laser System

Before we discuss suitable laser systems, we collect here some useful formulas for the calculation of luminosity. There are major differences, as to be expected, for continuous and pulsed lasers.

4.6.1 Luminosity for Continuous Lasers

The luminosity for the interaction of a continuous laser with a pulsed electron beam can be expressed (for round beams with $\sigma_x = \sigma_y = \sigma$) as follows [4, 14]

$$\mathcal{L} = \frac{1 + \cos \theta_0}{\sqrt{2\pi}} \frac{I_e}{e} \frac{P_L \lambda}{hc^2} \frac{1}{\sqrt{\sigma_e^2 + \sigma_\gamma^2}} \frac{1}{\sin \theta_0} \quad (18)$$

where θ_0 is the crossing angle of the two beams, I_e is the mean electron current, P_L is the power of the laser, λ is the wavelength of the laser, and σ_e and σ_γ are the rms beam sizes. The other symbols have the usual meaning.

For small crossing angle θ_0 and negligible electron beam size, in comparison with the size of the laser focus, one obtains

$$\mathcal{L} = 8.36 \cdot 10^{24} \text{ cm}^{-2} \text{ s}^{-1} \frac{\lambda}{\sigma_\gamma} \frac{I_e(\mu A) \cdot P_L(W)}{\theta_0(rad)} \quad (19)$$

With the following parameter settings

$$\begin{aligned} \theta_0 &= 0.010 \text{ rad} \\ \lambda &= 1.064 \text{ } \mu\text{m} \\ \sigma_\gamma &= 50 \text{ } \mu\text{m} \\ P_L &= 1.0 \text{ W} \\ I_e &= 45 \text{ } \mu\text{A} \end{aligned}$$

we obtain

$$\mathcal{L} = 0.80 \cdot 10^{27} \text{ cm}^{-2} \text{ s}^{-1} \quad (20)$$

Although the TESLA beam is not actually round as assumed in the derivation of equation 18, it does not matter here, since $\sigma_e \ll \sigma_\gamma$. More general expressions can be found in Ref. [16].

4.6.2 Luminosity for Pulsed Lasers

For pulsed lasers, one has the following expression for the luminosity [16]

$$\mathcal{L} = f_b N_e N_\gamma g \quad (21)$$

where f_b is the number of bunch crossings per second, N_e is the number of electrons per bunch, N_γ is the number of laser photons per laser pulse, and g is a geometry factor that accounts for the spatial overlap of the two beams

$$g = \frac{\cos^2(\theta_0/2)}{2\pi} \frac{1}{\sqrt{\sigma_{xe}^2 + \sigma_{x\gamma}^2} \sqrt{(\sigma_{ye}^2 + \sigma_{y\gamma}^2) \cos^2(\theta_0/2) + (\sigma_{ze}^2 + \sigma_{z\gamma}^2) \sin^2(\theta_0/2)}} \quad (22)$$

θ_0 is again the beam crossing angle. Vertical beam crossing (in the y-z plane) has been assumed, without loss of generality. For horizontal crossing, the roles of x and y are switched. For the derivation of equation 22, the transverse beam profiles have been assumed to be constant in the region of interest, which is a reasonable condition for our purposes.

For small crossing angle θ_0 :

$$g = \frac{1}{2\pi \sqrt{\sigma_{xe}^2 + \sigma_{x\gamma}^2} \sqrt{(\sigma_{ye}^2 + \sigma_{y\gamma}^2) + (\sigma_{ze}^2 + \sigma_{z\gamma}^2) (\theta_0/2)^2}} \quad (23)$$

If the transverse dimensions of the electron beam are small in comparison with the laser focus, as will generally be the case for TESLA, one obtains

$$g = \frac{1}{2\pi \sigma_{x\gamma} \sigma_{y\gamma} \sqrt{1 + (0.5 \theta_0 \sigma_{z\gamma} / \sigma_{y\gamma})^2}} \quad (24)$$

and

$$\mathcal{L} = \frac{\mathcal{L}_{max}}{\sqrt{1 + (0.5 \theta_0 \sigma_{z\gamma} / \sigma_{y\gamma})^2}} \quad (25)$$

For a given transverse size $\sigma_{x\gamma} \sigma_{y\gamma}$ of the laser focus, the luminosity reaches a maximum for small crossing angle and short laser pulses:

$$\mathcal{L}_{max} = \frac{f_b N_e N_\gamma}{2\pi \sigma_{x\gamma} \sigma_{y\gamma}} \quad (26)$$

The drop-off of $\mathcal{L}/\mathcal{L}_{max}$ with increasing laser pulse length and crossing angle is given in Table 5 for a laser focus $\sigma_{y\gamma} = 50 \mu m$.

$\sigma_{t\gamma}$	$\sigma_{z\gamma}$	$\mathcal{L}/\mathcal{L}_{max}$		
		3 mrad	10mrad	30mrad
(ps)	(mm)			
0	0	1.000	1.000	1.000
5	1.5	0.999	0.989	0.912
10	3.0	0.996	0.958	0.743
15	4.5	0.991	0.912	0.505
20	6	0.984	0.857	0.486
30	9	0.965	0.743	0.347
40	12	0.941	0.640	0.268
50	15	0.912	0.555	0.217
100	30	0.743	0.316	0.110
1000	300	0.110	0.033	0.011
10000	3000	0.011	0.003	0.001

Table 5: Luminosity $\mathcal{L}/\mathcal{L}_{max}$ vs. laser pulse length at different crossing angles θ_0 (for a laser focus $\sigma_{y\gamma} = 50 \mu m$).

For example, with a crossing angle of 10 mrad and a laser pulse length $\sigma_{t\gamma}$ of 16 ps , the luminosity will be about 90% of the maximum value.

At TESLA-500, with $f_b = 14100$ bunches per second, and $N_e = 2 \cdot 10^{10}$ electrons per bunch, we obtain

$$\mathcal{L}_{max} = 4.49 \cdot 10^{13} \frac{N_\gamma}{\sigma_{x\gamma} \sigma_{y\gamma} [\text{cm}^2]} s^{-1} \text{ cm}^{-2} \quad (27)$$

where N_γ is the number of laser photons per laser pulse, $\sigma_{x\gamma} \sigma_{y\gamma}$ is the transverse size of the laser beam at the beam crossing point, and the laser is fired with the same pulse repetition rate as the accelerator. Equation 27 remains unchanged for TESLA-800, as the average design current ($45 \mu\text{A}$) and the product $f_b \cdot N_e$ in equation 26 do not change between the two operating regimes of TESLA [1].

For a round laser focus with $\sigma_{x\gamma} = \sigma_{y\gamma} = 50 \mu\text{m}$, one obtains

$$\mathcal{L}_{max} = 1.12 \cdot 10^{31} \frac{j_\gamma [\mu\text{J}]}{\epsilon_\gamma [\text{eV}]} s^{-1} \text{ cm}^{-2} \quad (28)$$

where j_γ is the laser pulse energy and ϵ_γ is the energy of the laser photon. \mathcal{L}_{max} is listed in Table 6 for the standard TESLA reference parameters and several laser configurations.

λ (nm)	ϵ_γ (eV)	$\langle P_L \rangle$ (W)	j_γ (μJ)	\mathcal{L}_{max} ($10^{32} \text{ cm}^{-2} \text{ s}^{-1}$)		
				$25\mu\text{m}$	$50\mu\text{m}$	$100\mu\text{m}$
1064	1.165	1.0	71	27	6.8	1.7
532	2.33	0.5	35	6.8	1.7	0.43
266	4.66	0.2	14	1.4	0.34	0.085

Table 6: Compton luminosity at TESLA, for pulsed lasers of different beam size $\sigma_{x\gamma} = \sigma_{y\gamma}$.

4.6.3 Laser Emittance

As we have seen in the preceding chapters, the luminosity that can be achieved depends on the size of the laser focus at the IP. The size of the focus $\sigma_{x\gamma,y\gamma}$ can be expressed in terms of the emittance of the laser $\mathcal{E}_{x,y}$ and the angular half aperture $\theta_{x,y} = a_{x,y}/f$ of the converging laser beam

$$\sigma_{x\gamma,y\gamma} = \frac{\mathcal{E}_{x,y}}{\theta_{x,y}} = \frac{f}{a_{x,y}} \mathcal{E}_{x,y} \quad (29)$$

where $a_{x,y}$ and f are the effective half apertures and the focal length of the final lens system.

The best possible emittance of a perfect laser is limited by the laws of optics and depends on its wavelength

$$\mathcal{E}_{x,y}^{min} = \frac{\lambda}{4\pi} \quad (30)$$

In Table 7 we have listed the best possible laser emittance for several wavelengths and the associated minimal laser spot size that can be obtained with the beam crossing chamber shown in Fig. 14. This chamber can accommodate an angular aperture of $\theta_{x,y} = a_{x,y}/f = \pm 6mm/3000mm = \pm 2 \text{ mrad}$. For realistic lasers, one should of course expect somewhat larger emittances and spot sizes.

λ (nm)	$\mathcal{E}_{x,y}^{min} = \frac{\lambda}{4\pi}$ (mm · mrad)	$\sigma_{x\gamma,y\gamma}^{min}$ (μm)
1064	0.0847	42
532	0.0423	21
266	0.0212	11

Table 7: Minimal emittance for perfect lasers and minimal laser spot size for the beam crossing chamber shown in Fig. 14.

4.6.4 Laser for the Polarimeter

Compton scattering with typical continuous lasers in the 1-10 Watt range would be very slow at TESLA, due to the relatively low average current of a linear accelerator in comparison with storage rings such as HERA. This was already pointed out by Bardin et al. [4], who found that it would take a good fraction of an hour to collect enough statistics for a 1% measurement of the beam polarization.

It is possible to boost the available cw photon flux at the IP by several orders of magnitude. The laser cavity itself can be configured around the beam crossing chamber [19], or a separate resonant optical cavity, to which the feed laser is frequency locked [20]. These techniques would, however, require to operate the laser and associated equipment in the tunnel. Furthermore, these boosted cw laser scenarios would also lead to multiple Compton events per bunch, and therefore not offer any methodical advantage over pulsed lasers (see chapter 3.3).

As we have shown, it is possible to achieve very high luminosity at TESLA with short laser pulses in the 10 ps and 10 – 100 μJ regime, if the laser can be pulsed with a pattern that matches the peculiar pulse and bunch structure of TESLA.

A laser system with such exceptional properties is not commercially available, but has been developed at Max Born Institute for the TTF photoinjector gun at DESY, where it has been in operation for some time [17, 18]. This multi-stage solid-state laser system employs Nd:YLF and operates at a fundamental wavelength of 1047 nm in the infrared, which is converted in two steps to 2nd and 4th harmonic, for a final wavelength of 262 nm in the UV. The laser has delivered up to 250 μJ (IR) and 50 μJ (UV) per bunch, with associated pulse widths σ_t of 10 and 8 ps. The mean IR power is $\leq 2W$.

A variant of this TTF laser system would also be well suited for the Compton polarimeter. The luminosity that can be achieved with such a laser is typically six orders of magnitude higher than with a continuous laser of similar average power and emittance.

Table 8 gives tentative specifications for such a Nd:YLF solid-state laser system, as we propose for the Compton polarimeter. The laser pulse pattern should match that of the accelerator configuration, with a bunch spacing of 337 ns for TESLA-500 (within 950μs long pulse trains at 5 Hz), and 176 ns bunch spacing for TESLA-800 (within 860μs long pulse trains at 4 Hz) [1].

<i>configuration</i>	λ (nm)	ϵ_γ (eV)	$\langle P_L \rangle$ (W)	j_γ (μJ)	$\sigma_{t\gamma}$ (ps)	f_b (Hz)
<i>TESLA – 500</i>	524	2.37	0.5	35	10	14100 = 5 · 2820
<i>TESLA – 800</i>	1047	1.18	1.0	71	10	19544 = 4 · 4886
<i>Giga – Z</i>	262	4.74	0.2	14	10	?

Table 8: Tentative polarimeter laser specifications for TESLA-500, TESLA-800, and Giga-Z. P_L is the average laser power, j_γ the pulse energy, $\sigma_{t\gamma}$ the pulse length, and f_b is the total number of laser pulses per second.

4.7 Event Rates and Statistical Errors

For the determination of event rates and statistical errors, we will use the reference parameters listed in Table 9. In order to be consistent with the cross sections in Fig. 4-6, we list the wavelengths for a Nd:YAG laser. The wavelengths of the Nd:YLF laser are only slightly different. Not explicitly listed are the crossing angle $\theta_0 = 10 \text{ mrad}$ and the size of the laser focus $\sigma_{x\gamma} = \sigma_{y\gamma} = 50 \text{ }\mu\text{m}$, which are assumed to be common for all configurations.

configuration	E_0 (GeV)	$\langle I_e \rangle$ (μA)	λ (nm)	ϵ_γ (eV)	$\langle P_L \rangle$ (W)	j_γ (μJ)	\mathcal{L} ($10^{32} \text{ cm}^{-2} \text{ s}^{-1}$)
TESLA-500	250	45	532	2.33	0.5	35	1.5
TESLA-800	400	45	1064	1.165	1.0	71	6.0
Giga-Z	45.6	45	266	4.66	0.2	14	0.2

Table 9: Reference parameters for statistical tables.

The following Tables 10-12 list the binned cross sections and event rates in the electron detector for the three reference configurations of Table 9. As these events are bunched and recorded as analog signals at the bunch crossing frequency, there is no problem with apparently high rates, as we do not actually count individual events.

The longitudinal beam polarization P is determined from the experimental asymmetry $(N_1 - N_2)/(N_1 + N_2)$ of two measurements N_1 and N_2 with different helicity configurations (see Chapter 3.1, we assume here perfect laser polarization):

$$P = \frac{1}{A} \frac{N_1 - N_2}{N_1 + N_2} \quad (31)$$

where A is the cross section asymmetry or analyzing power defined in Equation 12, and N_1 and N_2 are the event statistics of the two measurements, normalized to the same integrated luminosity. The statistical error of the measured beam polarization follows through error propagation from $\Delta N_1 = \sqrt{N_1}$ and $\Delta N_2 = \sqrt{N_2}$:

$$\frac{\Delta P}{P} = \frac{1}{\sqrt{\sum_i w_i (N_{1i} + N_{2i})}} = \frac{1}{\sqrt{\Delta t \sum_i w_i R_i}} \quad (32)$$

where $R_i = (N_{1i} + N_{2i})/\Delta t$ is the event rate in energy bin i , Δt is the measurement time required for a certain statistical precision $\Delta P/P$ of the beam polarization, w_i are statistical weights to be defined below, and the sum \sum_i is over all energy bins i of interest.

$$w_i = \frac{1}{1 + P^{-2} A_i^{-2}} \quad (33)$$

The analyzing power A_i for each bin and the associated statistical weights w_i for a beam polarization $P = 0.80$ are also given in Tables 10-12. Furthermore, we list the statistical errors $\Delta P/P$ of the measured beam polarization which are calculated from equation 32 for a measurement duration Δt of 1 second.

We conclude from these numbers that genuine statistical errors originating from the Compton event statistics will be exceedingly small and likely negligible in comparison with systematic effects. Some systematic effects may, however, mimic statistical errors due to their more or less random behavior. Examples are fluctuations in the bunch charge of the machine, in the intensity and timing of the laser pulses, and baseline noise from a variety of sources. Their effect on the measurements can and must be reduced through suitable efforts. The bunch charge of the electron beam and the intensity and timing of the laser should be measured and recorded for each micropulse, so that the measured Compton signals can be properly normalized. Equally important is to monitor and record baseline variations under realistic operating conditions. Beam-related background can be determined easily from measurements with blocked or suppressed laser beam. Electronic noise generated by the firing of the laser can also be measured and accounted for.

<i>bin</i> #	min x_d (mm)	max x_d (mm)	E/E_0 low	E/E_0 high	Analyzing Power	Stat. Weight	$\langle d\sigma/dE \rangle dE$ (mbarn)	Rate (MHz)
1	-85	-90	0.089	0.094	-	-	-	-
2	-80	-85	0.094	0.100	-	-	-	-
3	-75	-80	0.100	0.107	0.927	0.355	3.35	0.503
4	-70	-75	0.107	0.115	0.812	0.297	3.79	0.568
5	-65	-70	0.115	0.123	0.687	0.232	3.92	0.588
6	-60	-65	0.123	0.134	0.554	0.165	4.14	0.621
7	-55	-60	0.134	0.146	0.415	0.099	4.37	0.655
8	-50	-55	0.146	0.161	0.268	0.044	4.70	0.705
9	-45	-50	0.161	0.178	0.114	0.008	5.10	0.765
10	-40	-45	0.178	0.201	-0.044	0.001	5.57	0.835
11	-35	-40	0.201	0.229	-0.203	0.026	6.28	0.943
12	-30	-35	0.229	0.268	-0.355	0.075	7.25	1.087
13	-25	-30	0.268	0.321	-0.489	0.133	8.74	1.311
14	-20	-25	0.321	0.401	-0.577	0.176	11.28	1.692
all	-20	-90	0.089	0.401			68.49	10.273
Statistical Error for $\Delta t = 1$ second:							$\Delta P/P = 0.89 \cdot 10^{-3}$	

Table 10: Event rates and statistical error for TESLA-500.

<i>bin</i> #	min x_d (mm)	max x_d (mm)	E/E_0 low	E/E_0 high	Analyzing Power	Stat. Weight	$\langle d\sigma/dE \rangle dE$ (mbarn)	Rate (MHz)
1	-85	-90	0.089	0.094	-	-	-	-
2	-80	-85	0.094	0.100	-	-	-	-
3	-75	-80	0.100	0.107	-	-	-	-
4	-70	-75	0.107	0.115	-	-	-	-
5	-65	-70	0.115	0.123	0.966	0.374	0.36	0.217
6	-60	-65	0.123	0.134	0.892	0.337	5.57	3.340
7	-55	-60	0.134	0.146	0.746	0.263	5.78	3.469
8	-50	-55	0.146	0.161	0.587	0.181	6.13	3.676
9	-45	-50	0.161	0.178	0.414	0.099	6.54	3.926
10	-40	-45	0.178	0.201	0.228	0.032	7.02	4.213
11	-35	-40	0.201	0.229	0.031	0.001	7.79	4.677
12	-30	-35	0.229	0.268	-0.169	0.018	8.85	5.309
13	-25	-30	0.268	0.321	-0.357	0.075	10.53	6.319
14	-20	-25	0.321	0.401	-0.502	0.139	13.49	8.093
all	-20	-90	0.089	0.401			72.06	43.239
Statistical Error for $\Delta t = 1$ second: $\Delta P/P = 0.45 \cdot 10^{-3}$								

Table 11: Event rates and statistical error for TESLA-800.

<i>bin</i> #	min x_d (mm)	max x_d (mm)	E/E_0 low	E/E_0 high	Analyzing Power	Stat. Weight	$\langle d\sigma/dE \rangle dE$ (mbarn)	Rate (MHz)
10	-40	-45	0.178	0.201	-	-	-	-
11	-35	-40	0.201	0.229	-	-	-	-
12	-30	-35	0.229	0.268	0.794	0.287	19.67	0.590
13	-25	-30	0.268	0.321	0.514	0.144	24.19	0.726
14	-20	-25	0.321	0.401	0.115	0.008	26.70	0.801
all	-20	-90	0.089	0.401			70.56	2.117
Statistical Error for $\Delta t = 1$ second: $\Delta P/P = 1.88 \cdot 10^{-3}$								

Table 12: Event rates and statistical error for Giga-Z.

4.8 Systematic Errors

A detailed treatment of systematic errors is beyond the scope of this note. We will only indicate some of the major instrumental issues and refer to other work on the subject [5, 21, 22, 23, 15]. Systematic effects from accelerator alignment, beam-beam interaction, bremsstrahlung background and radiative corrections have already been discussed. We expect a performance similar to the SLD polarimeter, with an overall precision of $\Delta P/P \sim 0.5\%$ for the measurement of the beam polarization.

4.8.1 Detector calibration and linearity

The analyzing power of a particular channel of the detector array depends in a well determined way on the Compton kinematics and its momentum acceptance in the spectrometer and is given in Tables 10-12 for a perfect dipole spectrometer and a detector with a uniform and linear response. A full-featured Monte Carlo description of the SLD polarimeter, which included an EGS shower simulation (they used a $1.2 X_0$ lead preradiator in front of the detector array) and a detailed simulation of the Cerenkov light transport, produced a detector response function which modified the effective analyzing power by $\sim 1\%$ [22, 23]. With the high rates we expect for the TESLA polarimeter, we can eliminate the preradiator and associated smearing effects (except for the window material of the electron exit chamber). Furthermore, complications associated with quadrupole fields in the SLD polarimeter spectrometer do not matter for the TESLA polarimeter, which employs effectively only dipoles. The quadrupole QFC1 shown in Fig. 2 has no important effect on the trajectories, as was shown in Fig. 8.

A simple but important feature of the SLD detector array was its ability to perform occasional table scans, whereby the individual detector channels could be calibrated and compared with each other. This procedure provides an important check on the reliability of the simulation and should also be employed at TESLA. The systematic uncertainty $\Delta P/P$ in the beam polarization measurement associated with such spectrometer calibrations was estimated to be 0.29% for the SLD polarimeter [5, 22, 23].

One of the most important instrumental issues is the degree of linearity of the analog signal, from which the asymmetry is formed, in relation to the particle flux entering the detector channel. It involves the Cerenkov detector response and also the photomultiplier, electronics and readout chain. This complex consumed the lion's share at 0.5% of the overall systematic error budget of 0.67% for the SLD polarimeter [5, 22, 23].

For the TESLA polarimeter one should aim to develop a suitable laser-based light injection system that can test the linearity of the entire system to high precision. This should have a high priority in view of the impact it has on the ultimate precision of the polarization measurement.

A possible configuration for such a light injection system would be to extend the L-shaped gas channels of the Cerenkov detector shown in Fig. 9 into an inverted U-shape, with an additional mirror on the upstream end. This would facilitate light injection, e.g. with quartz fibers, from a point which is well protected from direct beam exposure.

4.8.2 Laser polarization

The circular polarization of the laser light will be monitored in the laser lab and also downstream from the Compton IP. This is done with standard optical techniques to a typical precision of 0.2% [14, 15, 21].

4.8.3 Cross checks

An ultimate test of the reliability of the measured beam polarization would need an independent and equally precise measurement technique. A different beam polarimeter concept based on Møller and Bhabha scattering has also been investigated [26]. As this method employs a thin ferromagnetic foil target in the beamline, it could not operate in conjunction with physics data taking, but intermittently, if it is located upstream of the e^+e^- detector. With a recently developed new target concept [27, 28], it is in principle also capable of reaching a precision of 0.5%.

The Compton polarimeter itself provides numerous cross checks, as it can be operated in many different configurations, with different laser wavelengths, with electron or photon detection, multiple- or single events. Already the standard measurement procedure provides several redundant results from the different electron detector channels, which can be compared with each other. Furthermore, there are four different helicity configurations of the electron and laser beam.

With the electron and positron beam both polarized, one can in principle determine their polarizations via the Blondel scheme, without dedicated polarimeters, from the physics detector data themselves, by measuring $\sigma(e_L^-, e_R^+)$, $\sigma(e_R^-, e_L^+)$, $\sigma(e_L^-, e_L^+)$, and $\sigma(e_R^-, e_R^+)$, for some process, e.g. polarized Bhabha scattering or many other channels.

4.9 Infrastructure and Utilities

4.9.1 Polarimeter Lab surface building

The laser and the electronics and data acquisition system (DAQ) should be located in a dedicated surface building (Polarimeter Lab) in close vicinity to the polarimeter site in the tunnel. This scenario provides access to all critical laser and electronic elements and minimizes the length of the laser beam transport and the cables. This scenario is therefore strongly preferred for technical as well as economical reasons.

Fig. 12 shows the major facilities of TESLA on the Ellershoop Campus. The boundaries of the campus intersect the electron and positron beams at a distance of 590 m (e^-) and 625 m (e^+) from the e^+e^- interaction point. With polarimeter surface buildings at the site boundaries, as indicated in the figure, one can obtain minimal path lengths through vertical shafts to the tunnel.

Each polarimeter lab could be similar in size and functionality to the existing TPOL polarimeter lab at HERA-West, which has air conditioned rooms for the laser and the electronics, a storage and workshop area, and a control room.

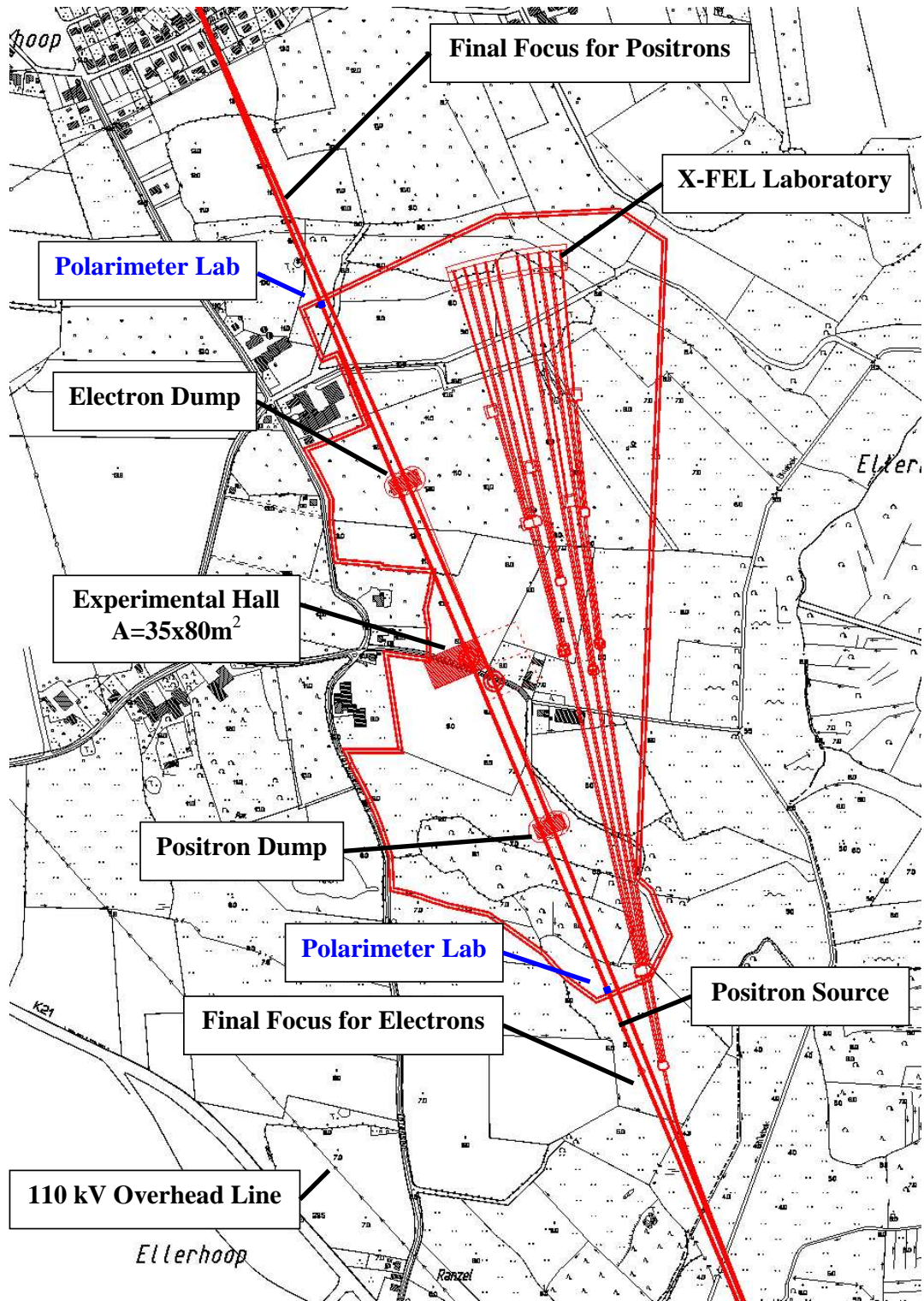


Figure 12. The Ellerhoop Campus.

4.9.2 Laser beam transport and diagnostics

The laser beam will be transported entirely under vacuum from the end of the laser table to the beam crossing chamber in the tunnel. The technology and hardware will be similar to existing facilities of the TPOL and LPOL polarimeters at HERA. An optional second laser beam line, equipped with optics for a different laser wavelength, would facilitate large changes of the beam energy of TESLA with minimal polarimeter downtime.

4.9.3 Tunnel layout

The principal polarimeter components in the tunnel and their locations along the beam-line are listed in Table 13. The lateral beam positions are indicated in Fig. 21.

	distance z (m)	
	from e^+e^- IP	
	e^-	e^+
	beam	beam
mirror box at laser beam entry into tunnel	-585	-620
mirror box at end of laser beam transport	-627	-627
beam crossing chamber (IP)	-630	-630
laser analyzer boxes	-633	-633
electron (positron) detector	-603.5	-603.5
optional photon detector	-560	-560

Table 13: Placement of polarimeter components in the tunnel.

4.10 Electronics and Data Acquisition

The fast electronics and data acquisition system for the TESLA polarimeter remains to be designed. It could be similar to the upgrade configuration for the TPOL polarimeter at HERA [24, 25], which is currently being implemented.

In the TPOL upgrade system, the analog signals are to be preamplified behind the photomultipliers and shaped at the end of the cables, before they are digitized. The ADC's (AD9042 from Analog Devices) are mounted on custom designed VME cards. They have a resolution of 12 bit and are running at 40 MHz (4 times the HERA clock frequency). The digitized information is stored in a pipeline on the board. The pipeline is 4 x 220 samples deep, thus allowing the storage of one full bunch train from HERA. A DAC system generates programmable digital levels and test pulses. TDC information with a resolution of 0.5 ns is also available.

The readout of the TPOL upgrade system is configured around a VME based PowerPC computer which is equipped with a MFCC (Multi-Function Computer Core) card developed by the CES company. The MFCC card communicates with the ADC card

through a dedicated high speed Altera bus (48 bits, 20 MHz). It can be programmed to perform simple logical operations and control functions.

The only motivation in describing the TPOL system here in such detail is to demonstrate that a suitable fast electronics and DAQ can be realized with existing technology. The actual design and implementation will depend on the rapidly evolving technical possibilities.

4.11 Cost

The estimated cost of the Compton Polarimeter, based on year 2000 prices, is summarized in Table 14. This cost table is figured on the assumption that the laser and the electronics and data acquisition system will be located in a dedicated surface building in close vicinity to the polarimeter site in the tunnel. Wherever applicable, costs have been scaled from experiences with similar existing facilities at DESY.

The incremental cost of an optional second laser beamline would be 150 kEuro per polarimeter.

The implementation of a polarimeter for the positron beam would of course be contingent upon a successful development of a polarized positron source.

	Cost Estimate (kEuro)
Surface Building	250
Laser	400
Vertical Shaft	25
Laser Beamline and Optics	125
Vacuum Chambers	75
e-Detector	50
Cables	10
Electronics and DAQ	165
Total for one beam	1100
Total for both beams	2200

Table 14: Cost estimate for Compton Polarimeters

5 Summary and Conclusion

The purpose of this study was to develop a suitable plan of a Compton beam polarimeter for TESLA, that meets the requirements of the physics and the machine for a precise, fast, non-invasive, flexible, robust and practical measurement.

We have examined the spin rotation properties and the infrastructure aspects of several potential site locations. We were able to identify an area in the beam delivery

system with an almost perfect configuration that requires only minimal adjustments for high-quality beam polarization measurements.

The laser envisaged for the polarimeter is similar to the laser which has been developed for the TTF photoinjector gun at DESY. It delivers very short pulses in the 10 ps, 10 – 100 μJ regime and can be operated with a pattern that matches the pulse and bunch structure of TESLA. This will permit very fast and accurate polarization measurements and an expeditious tune-up of the spin manipulators at the low-energy end of the linac. The performance of the polarimeter can be optimized by operating the laser at different wavelengths, depending on the TESLA energy regime.

Electron detection in the multi-event regime will be the principle operating mode of the polarimeter. Other detection methods are also possible, e.g. photon detection with an optional photon detector, or single-event detection for calibration purposes.

We expect an overall precision of $\Delta P/P \sim 0.5\%$ for the measurement of the beam polarization. As an example, Table 15 gives typical polarimeter parameters for TESLA-500. The performance is similar for other energy regimes of TESLA.

	e^+/e^- beam	laser beam
energy	250 GeV	2.3 eV
charge or energy/bunch	$2 \cdot 10^{10}$	35 μJ
bunches/sec	14100	14100
bunch length σ_t	1.3 ps	10 ps
average current(power)	45 μA	0.5 W
$\sigma_x \cdot \sigma_y$ (μm)	10 · 1	50 · 50
beam crossing angle	10 mrad	
luminosity	$1.5 \cdot 10^{32} cm^{-2} s^{-1}$	
cross section	$0.136 \cdot 10^{-24} cm^2$	
detected events/sec	$1.0 \cdot 10^7$	
detected events/bunch	$0.7 \cdot 10^3$	
$\Delta P/P$ stat. error/sec	negligible	
$\Delta P/P$ syst. error	$\sim 0.5\%$	

Table 15: Compton Polarimeter Parameters at 250 GeV

6 Acknowledgments

In the course of this study, we received valuable advice, information and help from many colleagues. In particular, we like to thank R. Brinkmann, J. Kuhlmann, O. Napoly, A. Petrov, S. Schreiber, H. Steiner, V. Telnov, N. Walker, and M. Woods.

References

- [1] *TESLA Technical Design Report*, DESY-2001-000, ECFA-2001-209, 2001.
- [2] K.P. Schüler, *Polarimeter Studies for TESLA*, in *Proceedings of the Linear Collider Workshop 2000*, Fermilab, Batavia, IL, USA, 2001.
- [3] R. Brinkmann et al., *Conceptual Design Report of a 500 GeV e^+e^- Linear Collider with integrated X-ray Laser Facility*, DESY-1997-048, 1997.
- [4] G. Bardin, C. Cavata and J.P. Jorda, *Compton Polarimeter studies for TESLA*, DESY print, TESLA 97-03.
- [5] M. Woods, *The Scanning Compton Polarimeter for the SLD Experiment*, SLAC-PUB-7319, 1996; 12th Int. Symposium on High-Energy Spin Physics (Spin96), NIKHEF, Amsterdam, Proceeding eds. C.W. de Jager et al., World Scientific, 1997, p. 843.
- [6] R. Alley, H. Aoyagi, J. Clendenin, J. Frisch, C. Garden, E. Hoyt, R. Kirby, L. Klaisner, A. Kulikov, R. Miller, G. Mulhollan, C. Prescott, P. Saez, D. Schultz, H. Tang, J. Turner, *The Stanford Linear Accelerator Polarized Electron Source*, Nucl. Instr. and Meth. A365 (1995) 1.
- [7] V.E. Balakin and A.A. Mikhailichenko, *The Conversion System for Obtaining High Polarized Electrons and Positrons*, Preprint INP 79-85, 1979.
- [8] K. Flöttmann, *Investigation Toward the Development of Polarized and Unpolarized High Intensity Positron Sources for Linear Colliders*, DESY-93-161, 1993.
- [9] I.F. Ginzburg, G.L. Kotkin, V.G. Serbo, and V.I. Telnov, Nucl. Instr. and Meth. 205 (1983) 47.
- [10] V.I. Telnov, Nucl. Instr. and Meth. A294 (1990) 72.
- [11] W.Y. Tsai, L.L. DeRaad, and K.A. Milton, Phys. Rev. D6 (1972) 1428; K.A. Milton, W.Y. Tsai, and L.L. DeRaad, Phys. Rev. D6 (1972) 1411.
- [12] H. Veltman, *Radiative corrections to polarized Compton scattering*, Phys. Rev. D40 (1989) 2810; Erratum Phys. Rev. D42 (1990) 1856.
- [13] M. L. Swartz, *A Complete Order- α^3 Calculation of the Cross Section for Polarized Compton Scattering*, Phys. Rev. D58:014010 (1998); hep-ph/9711447; SLAC-PUB-7701, 1997.
- [14] D.P. Barber et al., *The HERA polarimeter and the first observation of electron spin polarization at HERA*, Nucl. Instr. Meth. A329 (1993) 79.

- [15] M. Beckmann, S. Brauksiepe, F. Burkart, H. Fischer, J. Franz, F.H. Heinsius, K. Königsmann, F.M. Menden, C. Schill, J. Seibert, A. Simon, A. Borissov, W. Lorenzon, A. Most, S. Rudnisky, *The Longitudinal Polarimeter at HERA*, DESY-00-106, 2000.
- [16] T. Suzuki, *General formulae of luminosity for various types of colliding beam machines*, KEK-76-3 (1976).
- [17] I. Will, P. Nickles and W. Sandner, *A Laser System for the TESLA Photo-Injector*, internal design study, Max-Born-Institut, Berlin, 1994.
- [18] S. Schreiber, I. Will, D. Sertore, A. Liero and W. Sandner, *Running experience with the laser system for the RF gun based injector at the TESLA TEST Facility linac*, Nucl. Instr. and Meth. A445 (2000) 427.
- [19] M. Düren, *Prototype of an internal laser cavity system for polarized Compton backscattering*, Universität Bayreuth, internal report, Feb. 2000.
- [20] E. Barrelet, V. Brisson, M. Jacquet-Lemire, A. Reboux, C. Pascaud, Z. Zhang, F. Zomer, and the POL2000 group, *Proposal to Upgrade the Longitudinal Polarimeter*, DESY PRC 00-02, Oct. 2000.
- [21] M. Woods, K. Reeves, K. Moffeit, S. Ghosh, D. Calloway, *Compton Laser Analysis for the 94/95 SLD Run*, SLAC, SLD Note 246, April 1996.
- [22] M. Fero, P.L. Reinertsen, B.A. Schumm, M. Swartz, and E. Torrence, *Compton Polarization Measurement: 1995*, SLAC, SLD-Physics-Note-50, Nov. 1996.
- [23] E.C. Torrence, *Search for Anomalous Couplings in the Decay of Polarized Z Bosons to Tau Lepton Pairs*, MIT Ph.D. thesis, SLAC-Report-509, June 1997.
- [24] Polarization 2000 Group, V. Andreev et al., *Polarization 2000, proposal submitted to the PRC*, DESY PRC-98-07, June 1998.
- [25] Polarization 2000 Group, V. Andreev et al., *A Proposal for an Upgrade of the HERA Polarimeters for HERA 2000*, DESY PRC-99-04, Dec. 1998.
- [26] G. Alexander and I. Cohen, *Møller Scattering Polarimetry for High Energy e^+e^- Linear Colliders*, LC-DET-2000-046, Nov. 2000.
- [27] L.V. de Bever, J. Jourdan, M. Loppacher, S. Robinson, I. Sick, J. Zhao, *A target for precise Møller polarimetry*, Nucl. Instr. Meth. A400 (1997) 379.
- [28] M. Hauger, A. Honegger, J. Jourdan, G. Kubon, T. Petitjean, D. Rohe, I. Sick, G. Warren, H. Wöhrle, J. Zhao, R. Ent, J. Mitchell, D. Crabb, A. Tobias, M. Zeier, B. Zihlmann, *A High-Precision Polarimeter*, Submitted to Nucl. Instr. Meth., e-print archive: nucl-ex/9910013.

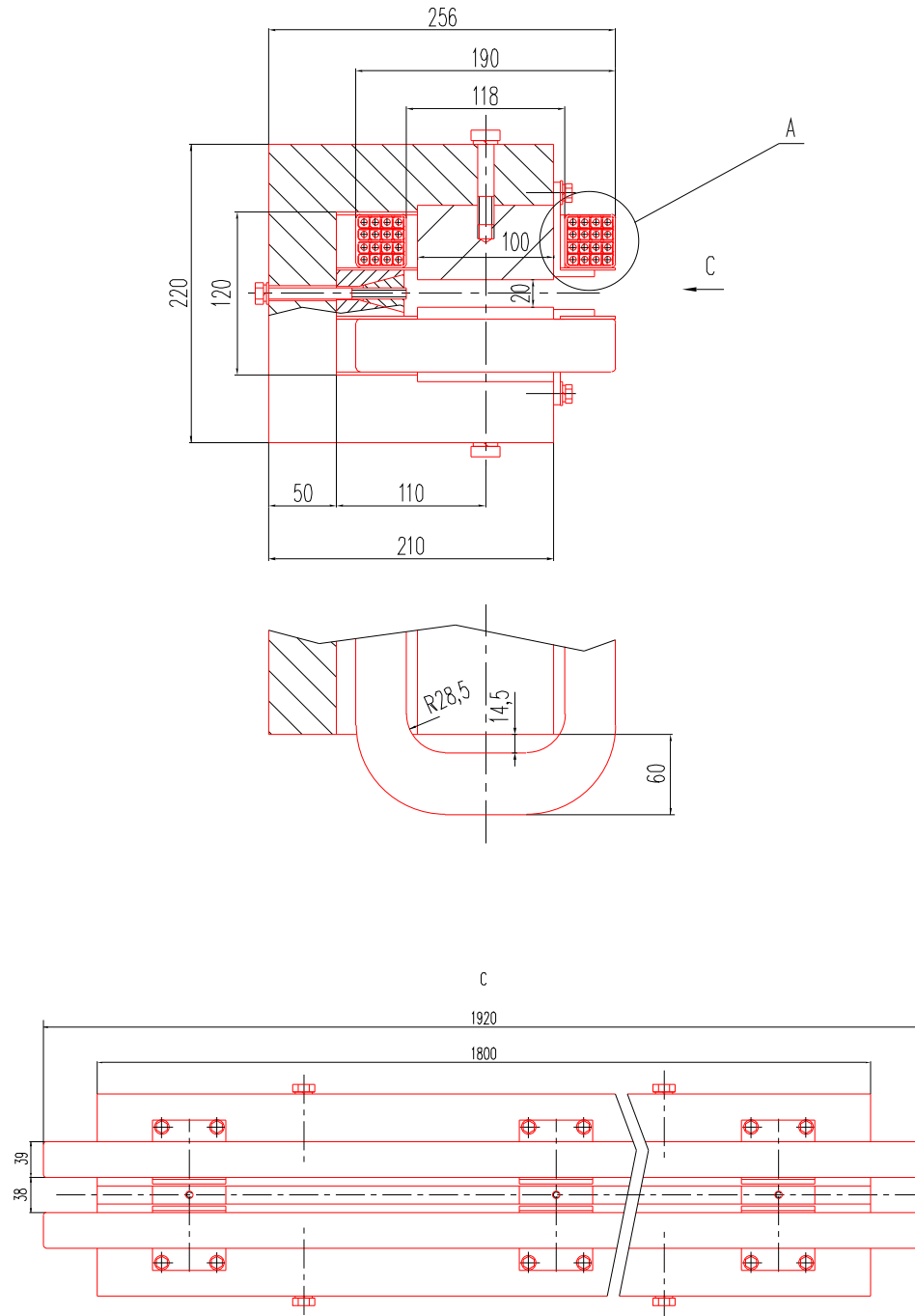


Figure 13. (a) Cross section (top) and (b) sideview (bottom) of the dipole BFCH0.

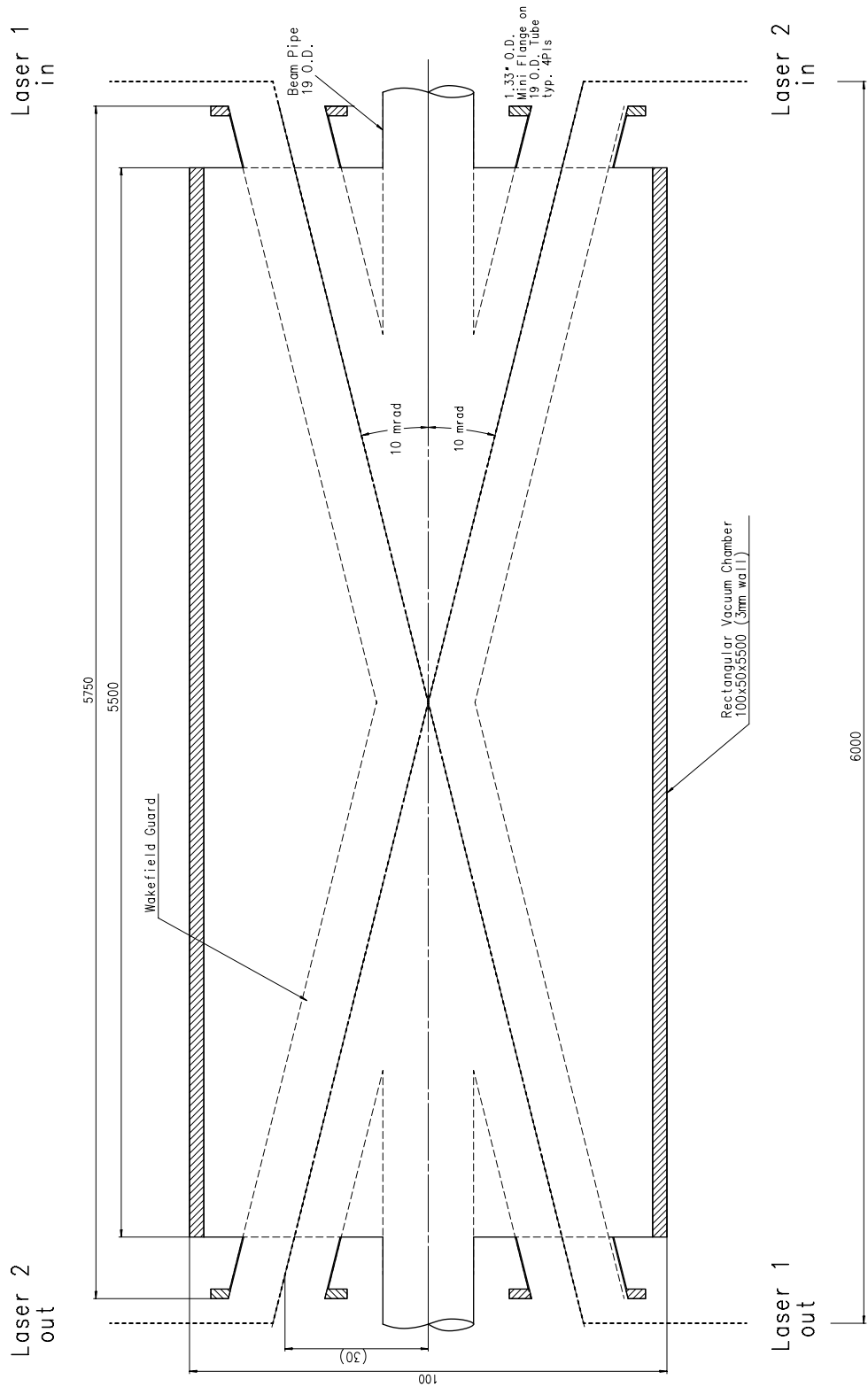
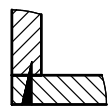
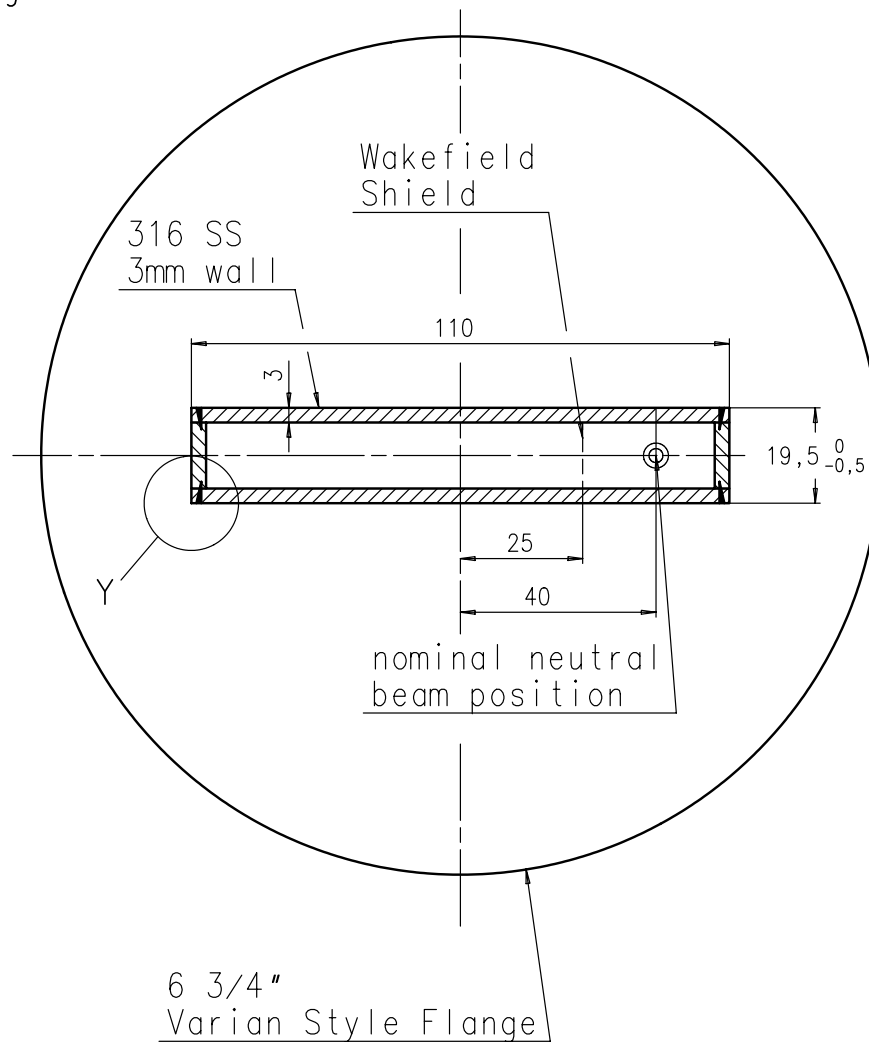


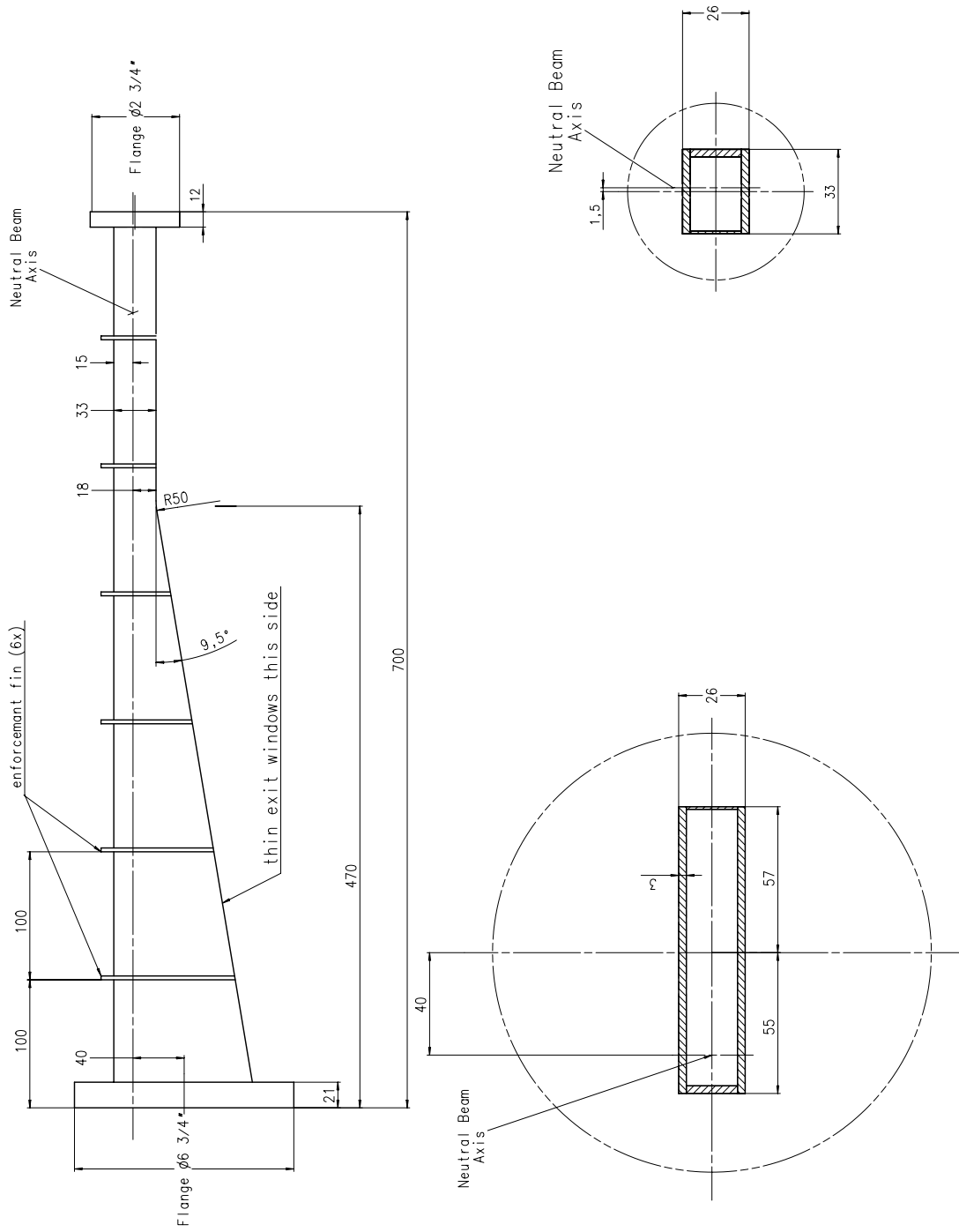
Figure 14. Laser beam crossing vacuum chamber.

TESLA Compton Polarimeter
Vacuum Chamber
Segment No. 9 and 10



Detail Y:
Laser Weld

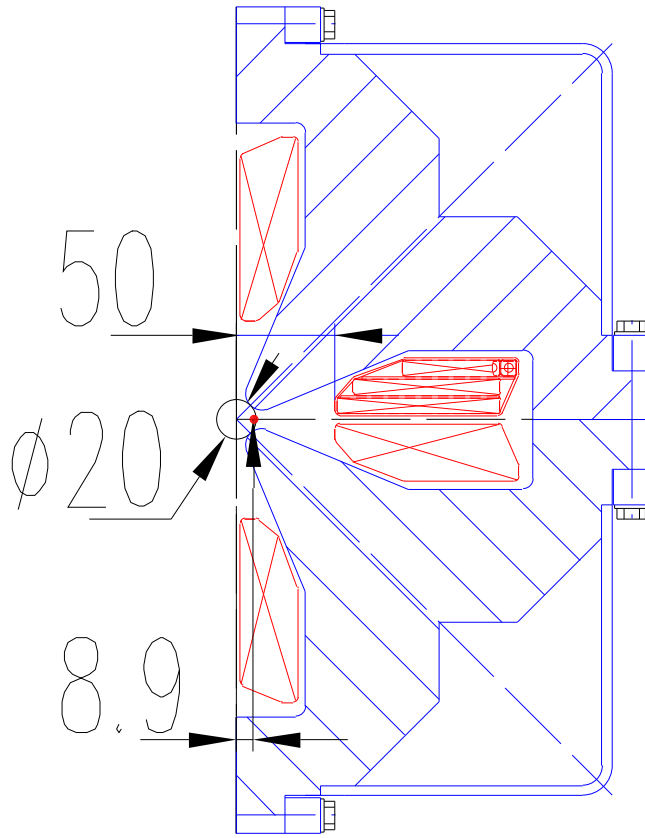
Figure 15. Dipole vacuum chamber: cross section of segment No. 9 and 10.



UPSTREAM FLANGE
6 3/4" O.D. VARIAN STYLE

DOWNSTREAM FLANGE
2 3/4" O.D. VARIAN STYLE

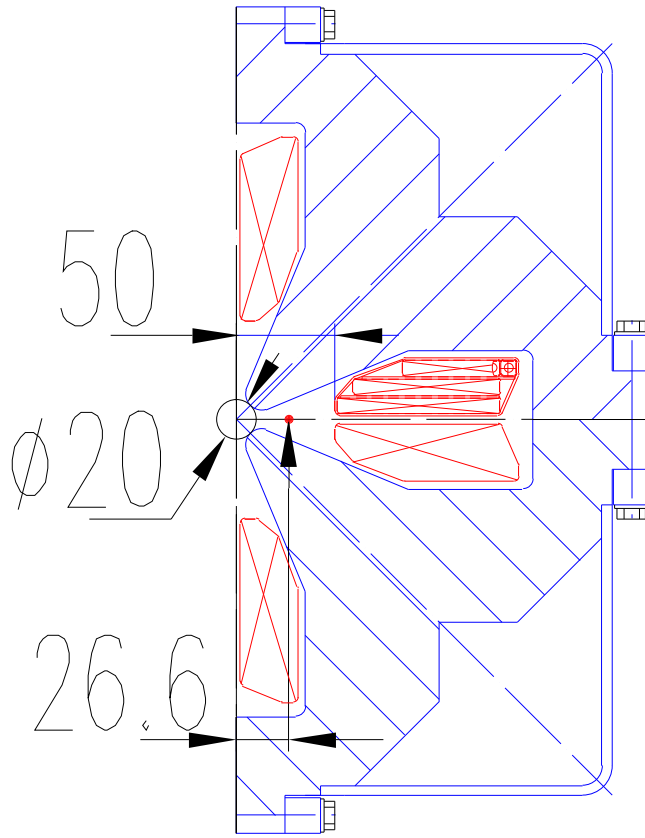
Figure 16. Electron exit vacuum chamber.



QFC2

at $z = -602.42$ m

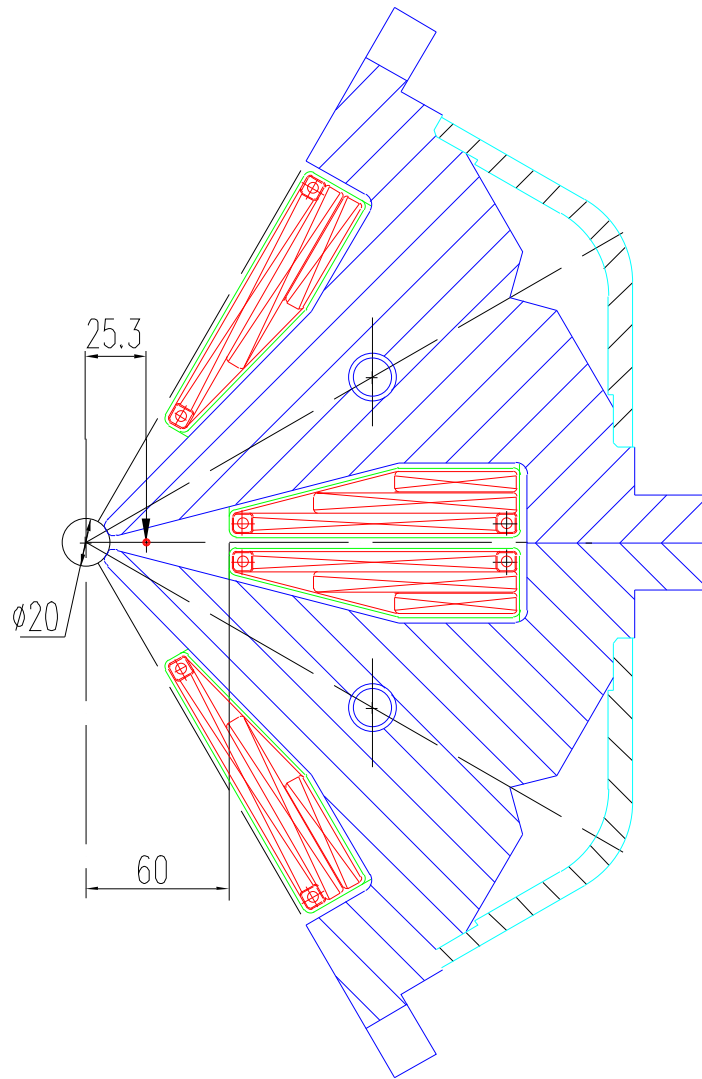
Figure 17. Neutral beam offset in the quadrupole QFC2.



QFC3

at $z = -579.42$ m

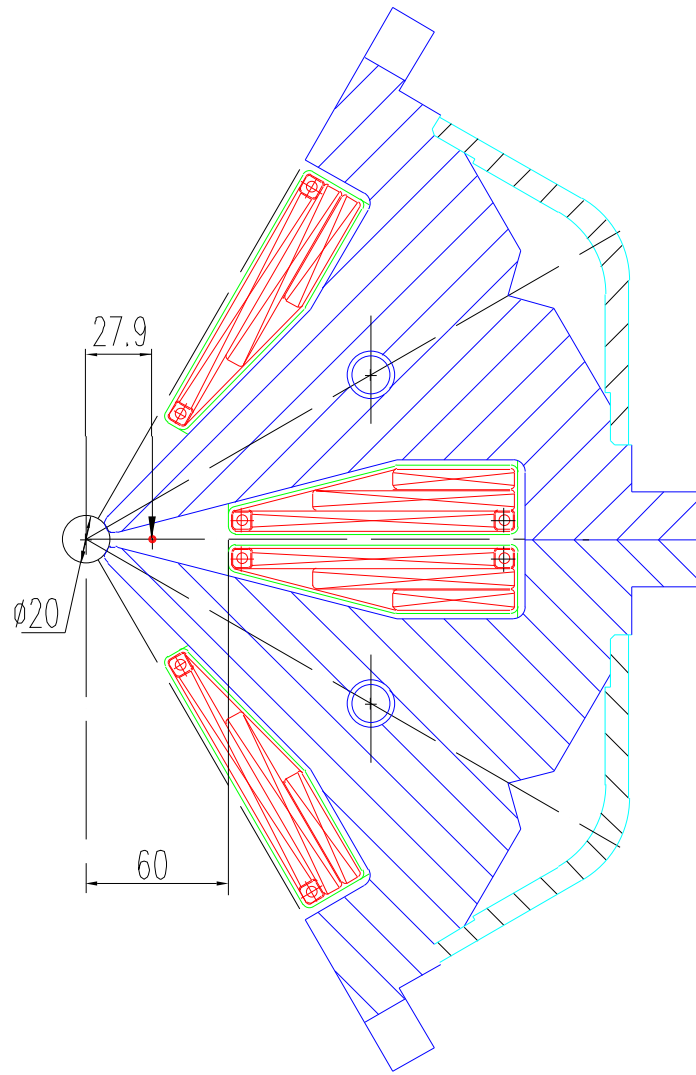
Figure 18. Neutral beam offset in the quadrupole QFC3.



SFCH

at $z = -581.12$ m

Figure 19. Neutral beam offset in the sextupole SFCH (-581.12m).



SFCH
 at $z = -577.72$ m

Figure 20. Neutral beam offset in the sextupole SFCH (-577.72m).

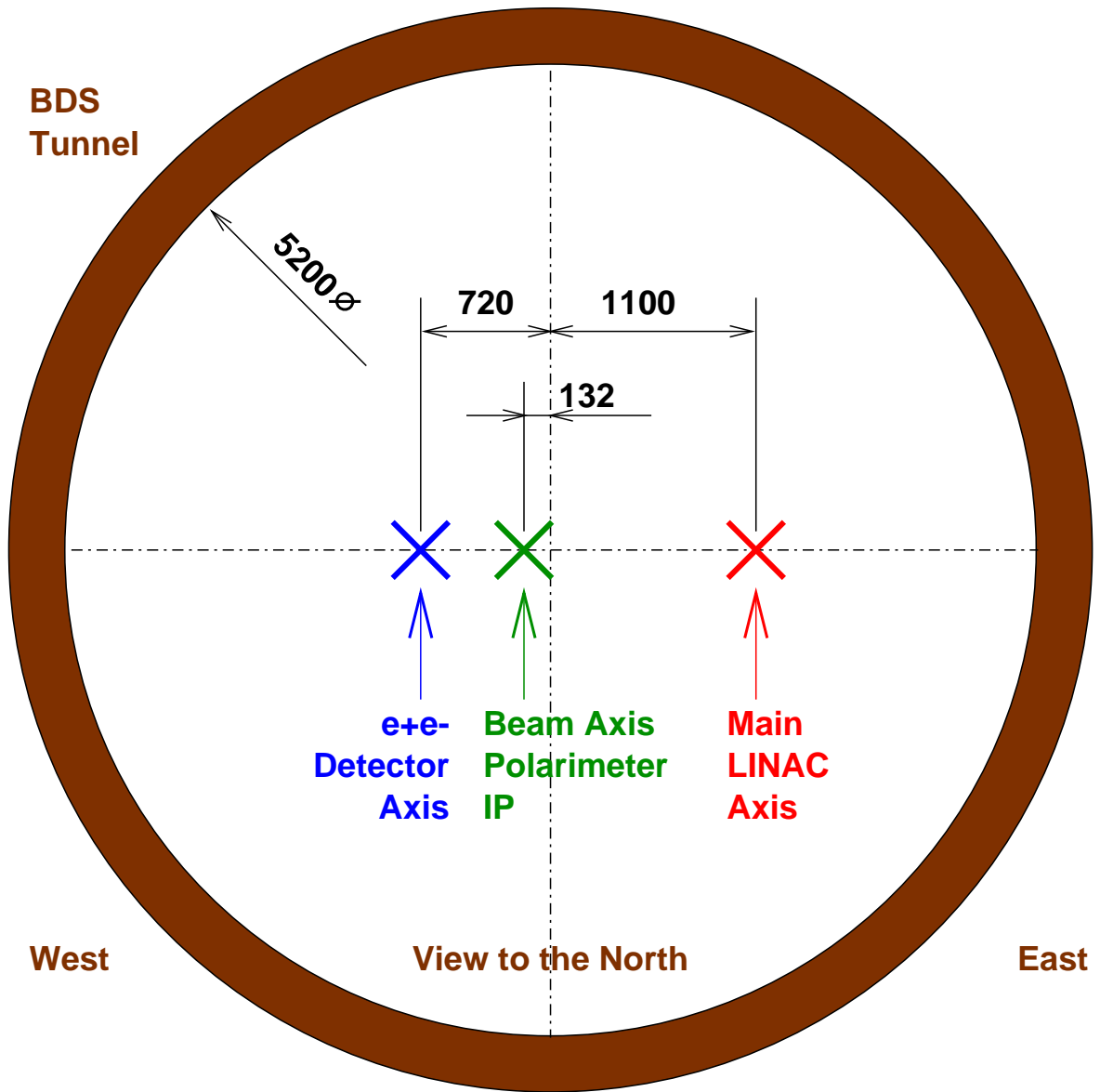


Figure 21. Tunnel cross section at the polarimeter.